Supporting Information

Significant Contribution of Single Atomic Mn Implanted in Carbon Nanosheets to High-performance Sodium-ion Hybrid Capacitors

Xiang Hu,[a,b] Genxiang Wang,[a] Junwei Li,[a] Junheng Huang,[a] Yangjie Liu,[a, b] Guobao Zhong,[a, b] Jun Yuan,[a, b] Hongbing Zhan[b] and Zhenhai Wen[a,*]

a CAS Key Laboratory of Design and Assembly of Functional Nanostructures, and Fujian Provincial Key Laboratory of Nanomaterials, Fujian Institute of Research on the Structure of Matter, Chinese Academy of Sciences, Fuzhou, Fujian 350002, China.

b College of Materials Science and Engineering, Fuzhou University, Fuzhou 350108, China

* Corresponding authors
E-mail: wen@fjirsm.ac.cn

Experimental Section

Chemicals: Manganous acetate (Mn(CH$_3$COO)$_2$·4H$_2$O, 99.99%), melamine (C$_3$H$_6$N$_6$, ≥ 99.5%) and polytetrafluoroethylene (PTFE) were purchased from Sigma-Aldrich. Ethanol (analytical reagent) and glucose (C$_6$H$_{12}$O$_6$, ≥ 99.5%) were purchased from Sinopharm Chemical Regent Co., Ltd., China. All reagents were of analytical grade and used without further purification.

Material synthesis: In a typical synthesis, 6 g of melamine, 12 g of PTFE, 0.25 mmol of Mn(CH$_3$COO)$_2$·4H$_2$O and a certain quantity of ethanol were mixed and grinded for about 1 h to obtain a homogenous precursor. Afterward, the mixture powder was loaded in a porcelain boat and firstly pyrolyzed at 450 °C for 2 h with a heating rate 3 °C min^{-1} from room temperature in Ar atmosphere, then the temperature was further increased to 800 °C with a heating rate 2 °C and maintained for 1 h. After cooled to room temperature, the obtained samples were denoted as MnSAs/NF-CNs. For comparison, NF-C was also prepared as the same procedure for MnSAs/NF-CNs except for the omissions of manganese salt. The N-C was synthesized as the same heat treatment procedure for MnSAs/NF-CNs but changing the precursor to 6 g of melamine and 300 mg glucose.

Materials characterization: The field emission scanning electron microscopy (FESEM, Hitachi SU-8020), transmission electron microscope (TEM, HRTEM, Tecnai F20), atomic force microscopy (AFM, Digital 407 Instruments, Version 6.12), X-ray di□raction (XRD, Miniflex 600 powder X-ray diffractometer with a Cu Kα radiation source), Raman spectrum (LabRam HR800), Electron paramagnetic resonance (EPR) spectra (Bruker-E500), thermogravimetric analysis (TGA, NETZSCH STA449F3) were employed to characterize the morphology, surface roughness, disordered structure and defects, and transition of the obtained products. Inductively coupled plasma optical emission spectrometry (ICP-OES, Varian 710) was used to measure the elemental content. Aberration-corrected high-angle annular darkfield scanning transmission electron microscope (HAADF-STEM) image was

recorded on a Titan Cubed Themis G2 300 operated at 80 keV. The specific surface area and pore size distributions were determined by the Nitrogen adsorption-desorption analysis at 77 K using an Intelligent Gravimetric Sorption Analyser (IGA100B). X-ray photoelectron spectroscopy (XPS) analysis was performed on an ESCALAB 250Xi spectrometer with an Al Kα X-ray source.

Electrochemistry characterization: These carbon electrodes were prepared by slurry (containing 80 wt. % active materials, 10 wt. % conductive carbon, and 10 wt. % sodium carboxymethyl cellulose) casting onto copper foil with blade coating technique, and then dried at 120 ℃ for 24 under vacuum. The average mass loadings of active materials are around 0.8-1.0 mg cm^{-2}. The sodium ion half-cell were assembled using 2032 coin-type cells with the as-prepared carbon electrodes as the working electrode, sodium slice as the counter electrode, Whatman glass fibers as separator, 1 M NaClO$_4$ in 1:1 v/v mixture of ethylene carbonate (EC) and dimethyl carbonate (DMC) acted as the electrolyte in a highly pure argon-filled glove box. Galvanostatic charge-discharge (GCD) tests were performed within the voltage range of 0.01-3.0V (vs Na/Na$^+$) by a LAND CT2001 (Wuhan, China) programmable battery tester at room temperature. After cycling test, the rate performance characteristics of the cells were continue evaluated at various current densities. The cyclic voltammetry (CV) profiles (0.01-3.0 V) and electrochemical impedance spectroscopy (at a frequency range from 0.01 Hz to 100 kHz) were carried out using a CHI660E electrochemical workstation. The galvanostatic intermittent titration technique (GITT) measurements were tested under constant-current conditions for 20 min at a constant current density of 0.2 A g^{-1} after the 50th cycles, followed by relaxation period of 2 h. The cycled cells of MnSAs/NF-CNs electrode were disassembled at different charging/discharging stages and the electrodes were washed with DMC to remove the electrolyte in the highly pure argon-filled glovebox. Then the naturally dried electrodes were conducted ex-situ Raman, XRD, XPS, TEM and SEM measurements.

The button cell-based SIHC full cell devices were assembled using the presodiation MnSAs/NF-CNs as battery-type anode and raw MnSAs/NF-CNs as capacitive-type cathode cathode with a mass ratio ranging from of 1:3 to 1:5. For the fabrication of the cathode, 80 wt% MnSAs/NF-CNs, 10 wt. % conductive carbon, and 10 wt% poly(vinyl difluoride) were dissolved in N-methyl pyrrolidone. The slurry was then coated onto an aluminum foil and dried at 100 °C overnight in a vacuum. Before the assembling of the full MnSAs/NF-CNs//MnSAs/NF-CNs SIHCs device, the anode was discharged-charged for ten cycles in half cell under 0.2 A g^{-1} and terminated at a sodiation state of 0.01 V. The energy (E, Wh kg^{-1}) and power densities (P, W kg^{-1}) of the SIHCs full-cells were calculated by integrating the galvanostatic discharge curves based on the total mass of both anode and cathode electrodes. It is worthy pointing out that the discharging process is almost a linear curve, therefore, the discharging energy density and power density can be calculated according to Eq. S1-S3, which was extensively used in previous works:[1]

$$E = \int_{t_1}^{t_2} V\,idt = \frac{1}{2} C\,(V_{max} + V_{min})(V_{max} - V_{min}) = \Delta V \times \frac{i}{m} \times t$$

(Equation S1)

$$P = \frac{E}{t} = \Delta V \times \frac{i}{m}$$

(Equation S2)

$$\Delta V = (V_{max} + V_{min})/2$$

(Equation S3)

where C($=[(i \times t)/m] \times [1/(V_{max}-V_{min})]$) is the capacitance of the SIHCs device, t_1 and t_2 are the start/end-of-discharge time (s), t (s) is the discharge time, i (A) is the charge/discharge current, m (g) is the total mass of active materials in both anode and cathode, V_{max} (V) is the initial discharge voltages excluding the IR drop and V_{min} (V) is the final discharge voltages.

Calculation Method: DFT calculations were used with periodic super-cells under the generalized gradient approximation (GGA) using the Perdew-Burke-Ernzerhof (PBE) function for exchange-correlation. The interaction of ion-electron is described by projected augmented wave (PAW). The Kohn-Sham orbitals were expanded in a plane-wave basis set

with a kinetic energy cutoff of 30 Ry and the charge-density cutoff of 300 Ry. The Fermi-surface effects has been treated by the smearing technique of Methfessel and Paxton, using a smearing parameter of 0.02 Ry. The Brillouin-zones were sampled with a k-point mesh of $2\times2\times1$. The calculation model of the pure carbon, N-C, NF-C, MnSAs/NF-CNs and MnN$_4$-C were constructed with 5×5 lateral periodicity. The vacuum layer was ~15 Å to decouple adjacent atomic slabs in the z direction. The nudged elastic band (NEB) method was used to evaluate the transition state and activation energy for one Na+ migrate from one hollow site in structure to another hollow site. The adsorption energy of Na is calculated by Equation

$$\Delta E_a = (E_{compound} - nE_{Na} - E_{str})/n \qquad \text{(Equation S4)}$$

where $E_{compound}$ is the total energy of the structure and nNa, E_{Na} is the energy of one Na atom, E_{str} is the energy of corresponding structure, and n corresponds to the number of Na atoms in the composite structure. Our DFT calculations were conducted by the Quantum ESPRESSO.[2]

XAFS measurements and analysis: XAFS data of Mn K-edge was collected at BL14W1 station in SSRF and 1W1B station in BSRF. The storage rings of SSRF and BSRF were operated at 3.5 GeV with the current of 300 mA and at 2.5 GeV with the current of 250 mA respectively. The acquired EXAFS data was processed according to the standard procedures using the ATHENA module implemented in the IFEFFIT software packages. The k^3-weighted EXAFS spectra were obtained by subtracting the post-edge background from the overall absorption and then normalizing with respect to the edge-jump step. Subsequently, k^3-weighted χ(k) data in the k-space ranging from 1.0 - 11.0 Å^{-1} was Fourier transformed to real (R) space using a hanning windows (d_k = 1.0 Å^{-1}) to separate the EXAFS contributions from different coordination shells.

EXAFS fitting details: To obtain the quantitative structural parameters around Mn atoms, least-squares curve parameter fitting was performed using the ARTEMIS module of IFEFFIT.[3] Effective scattering amplitudes and phase-shifts for the Mn-N and Mn-Mn pairs

were calculated with the ab initio code FEFF8.0.3. First of all, fits for the EXAFS data at Mn K-edge for Mn foil were performed. The coordination numbers of the first coordination shells were fixed as the nominal values, while the internal atomic distances R, Debye-Waller factor σ^2, and the edge-energy shift E_0 were allowed to run freely. The amplitude reduction factor S_0^2 was also treated as adjustable variable and the obtained value for foil counterpart was fixed in fitting the subsequent Mn edge data for samples. The fit was done on the k^3-weighted EXAFS function $\chi(k)$ data from 1.0 to 11.0 $Å^{-1}$ in the R-range of 1.0 - 2.0 Å. The coordination numbers N, interatomic distances R, Debye-Waller factor σ^2 and the edge-energy shift ΔE_0 for were allowed to run freely. Following the above fitting strategy, we got satisfactory curve-fitting results.

Calculation of the b Value and Capacitive Contribution: The measured current of CV curves could be separated into two types of charge storage for Na-ion batteries electrode materials, i.e., surface capacitive dominated processes (surface redox pseudocapacitance and double-layer capacitance) and diffusion-controlled processes (Na^+ insertion/extraction). Generally, the charge storage kinetics mechanism can be investigated by the power-law relationship between the measured current density (i) and the sweep rate (*v*) based on the following formulas:[4]

$$i = a\, v^b \qquad \text{(Equation S5)}$$

$$\log(i) = b\log(v) + \log(a) \qquad \text{(Equation S6)}$$

where a and b are variables, and the b value of 0.5 denotes a totally faradaic intercalation process and the b-value of 1 indicates an ideally capacitive contribution process. Quantitatively, the mixed behaviors can be further distinguished by separating the current response (i) at a specific potential (V) according to the following equations:[5]

$$i(V) = k_1 v + k_2 v^{1/2} \qquad \text{(Equation S7)}$$

$$i(V)/v^{1/2} = k_1 v^{1/2} + k_2 \qquad \text{(Equation S8)}$$

where both k_1 and k_2 are constant values, k_1v and $k_2v^{1/2}$ represent the contribution from surface capacitive behavior and contribution of diffusion-dominated reaction, respectively.

Galvanostatic intermittent titration (GITT) measurement: Ion diffusivity (D_{Na+}) of electrode materials is a crucial factor for batteries, which relates immediately to their rate performance. The value of D_{Na+} can be calculated from the GITT potential profiles according to the simplified Fick's second law with the following equation:[6]

$$D = \frac{4}{\pi\tau}\left(\frac{m_B V_M}{M_B S}\right)^2 \left(\frac{\Delta E_s}{\Delta E_\tau}\right)^2 \qquad \text{(Equation S9)}$$

where m_B is the electrode active mass, S (cm^2) represents the geometric area of electrode, ΔE_s denotes the quasi-thermodynamic equilibrium potential difference between before and after the current pulse, τ is the duration of the current pulse, ΔE_τ is the change of voltage during the current pulse. M_B (g mol^{-1}) and V_M (cm^3 mol^{-1}) are the molecular weight and molar volume of carbon material. The relative value of M_B/V_M can be obtained from the density of carbon materials, which is calculated by the following equation:

$$\rho = \frac{1}{V_{total} + \dfrac{1}{\rho_{carbon}}} \qquad \text{(Equation S10)}$$

where ρ (g cm^{-3}) is the density of carbon materials, V_{total} (cm^3 g^{-1}) is the total pore volume determined from the nitrogen isotherm, and ρ_{carbon} is the true density of carbon (2 g cm^{-3}).
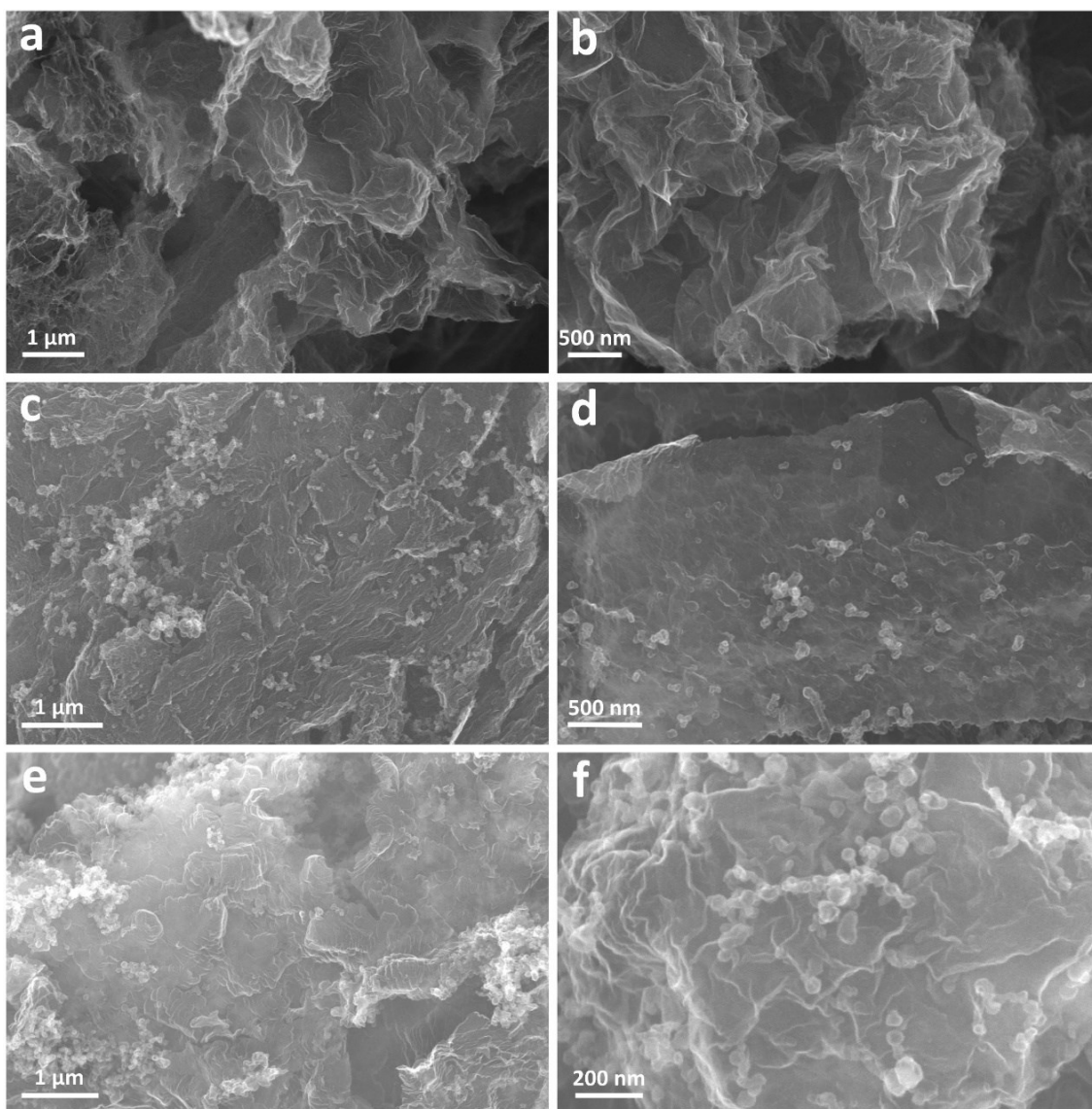
Figure S1. FESEM images of control samples of MnSAs/NF-CNs obtained through different pyrolysis temperature: (a, b) 450℃, (c, d) 550℃ and (e, f) 650℃.

During the initially thermal treatment, the melamine could be polymerized and pyrolyzed into graphitic carbon nitride, which function as the 2D sacrifice template for the following carbon nanosheets. With the pyrolysis temperature increasing, the PTFE and melamine as the well foaming reagent were gradually decomposed along with the release a lot of F, N - containing gas, and therefore cause high efficient doping of fluorine and nitrogen around the isolated Mn atoms in the porous carbons nanosheets.
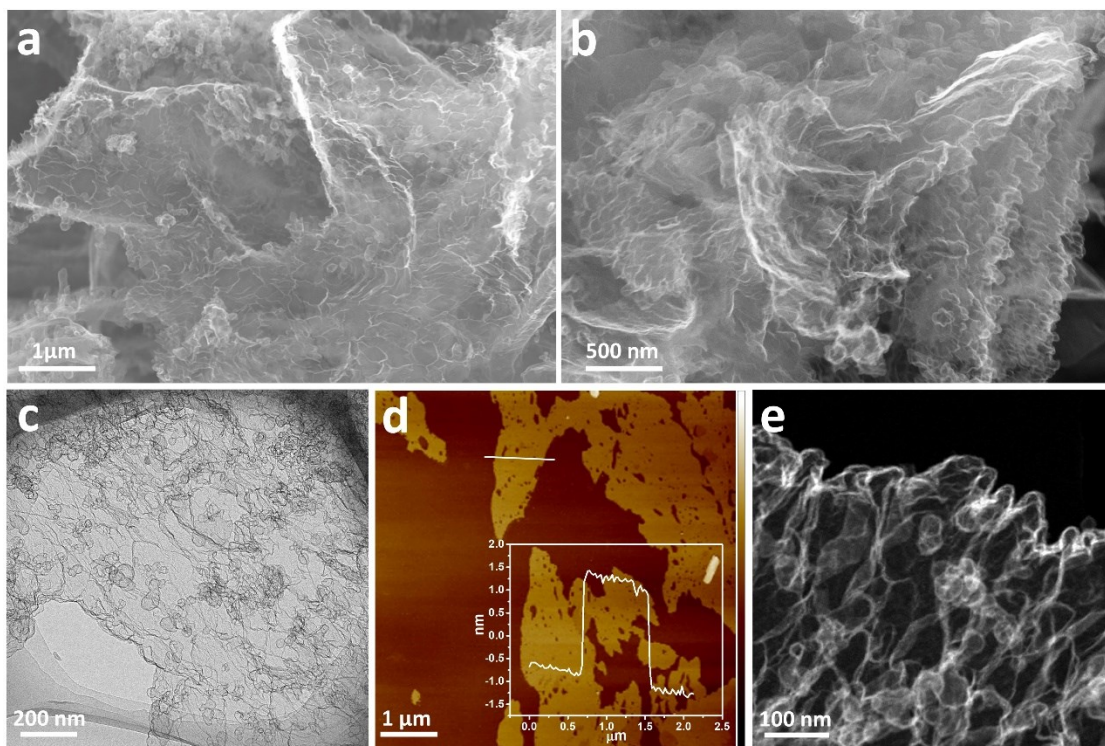
Figure S2. (a, b) FESEM, (c) TEM, (d) AFM and (e) HAADF-STEM images of MnSAs/NF-CNs.
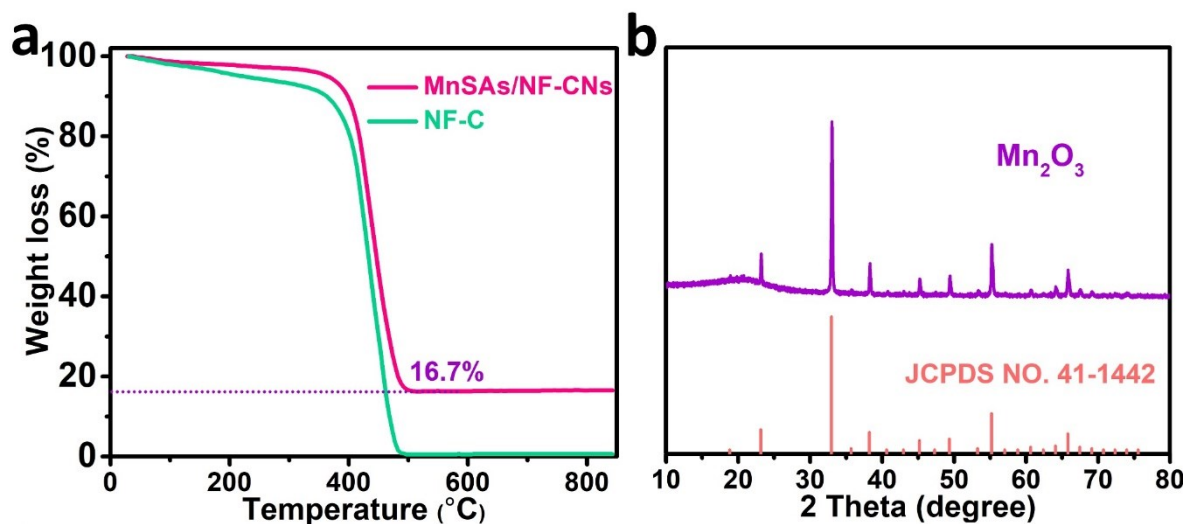
Figure S3. (a) TGA curves of MnSAs/NF-CNs and NF-C obtained at air atmosphere with a heating rate of 10 °C min^{-1}. (b) XRD pattern of the residual material after TGA test of MnSAs/NF-CNs.

TGA analysis:

From the TGA curves, the total weight loss of the MnSAs/NF-CNs was determined to be 83.3% after 500 °C. The XRD pattern of the MnSAs/NF-CNs shows that the residue is Mn_2O_3 after TGA test. Therefore, the weight loss of the MnSAs/NF-CNs can be attributed to the decomposition of carbonaceous nanosheets and the oxidation of Mn single atoms into Mn_2O_3, respectively. The total reaction can be simply written as:

$$C + O_2 \rightarrow CO_2 \qquad (1)$$
$$4\,Mn + 6\,O_2 \rightarrow 2\,Mn_2O_3 \qquad (2)$$

Based on the final residual weight of the Mn_2O_3, it can be calculated that the mass content of Mn single atoms in MnSAs/NF-CNs to be about 11.6%.
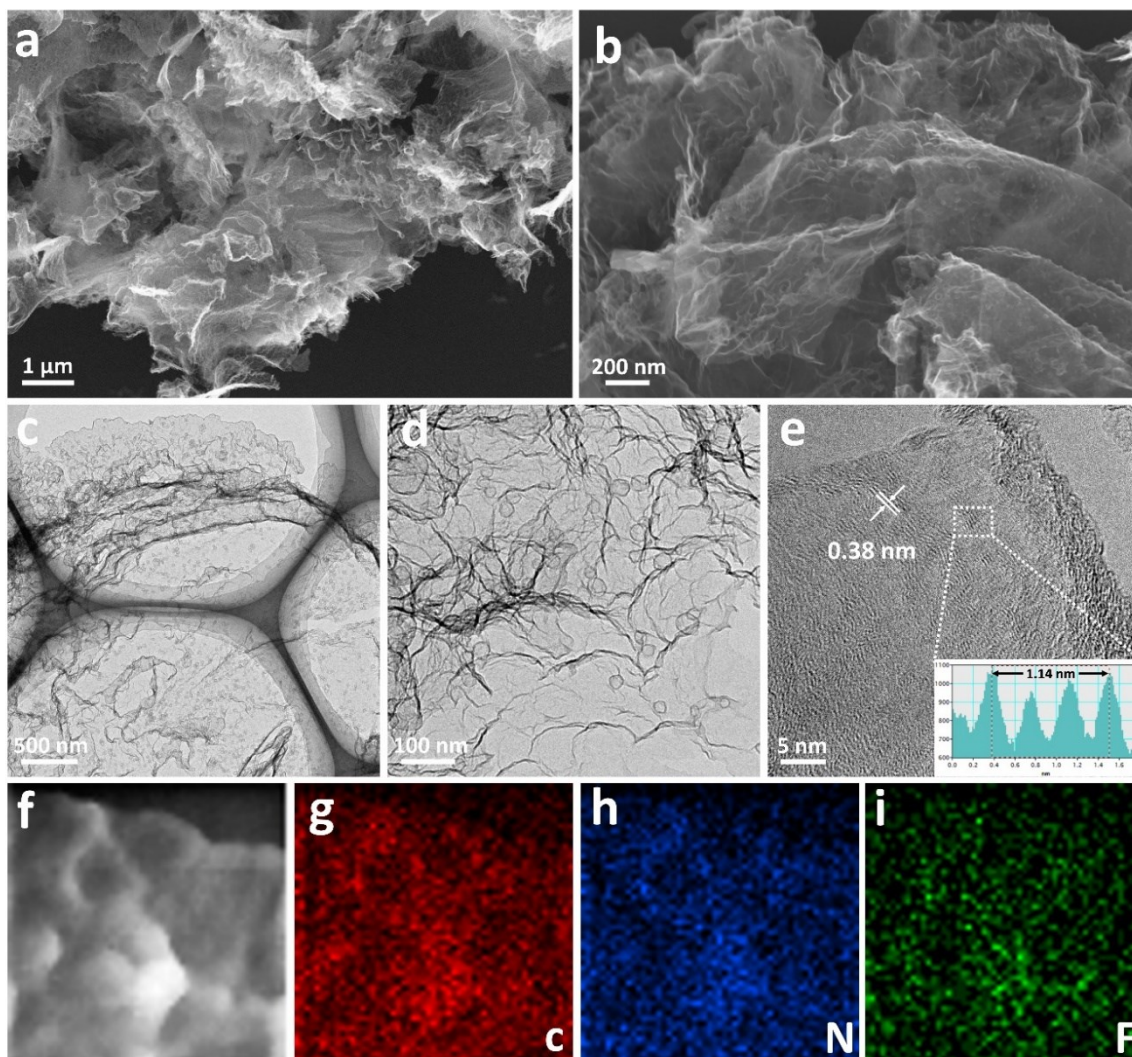
Figure S4. (a, b) FESEM, (c, d) TEM, (e) HRTEM, (f-i) HAADF-STEM image and EDS elemental mappings of NF-C.
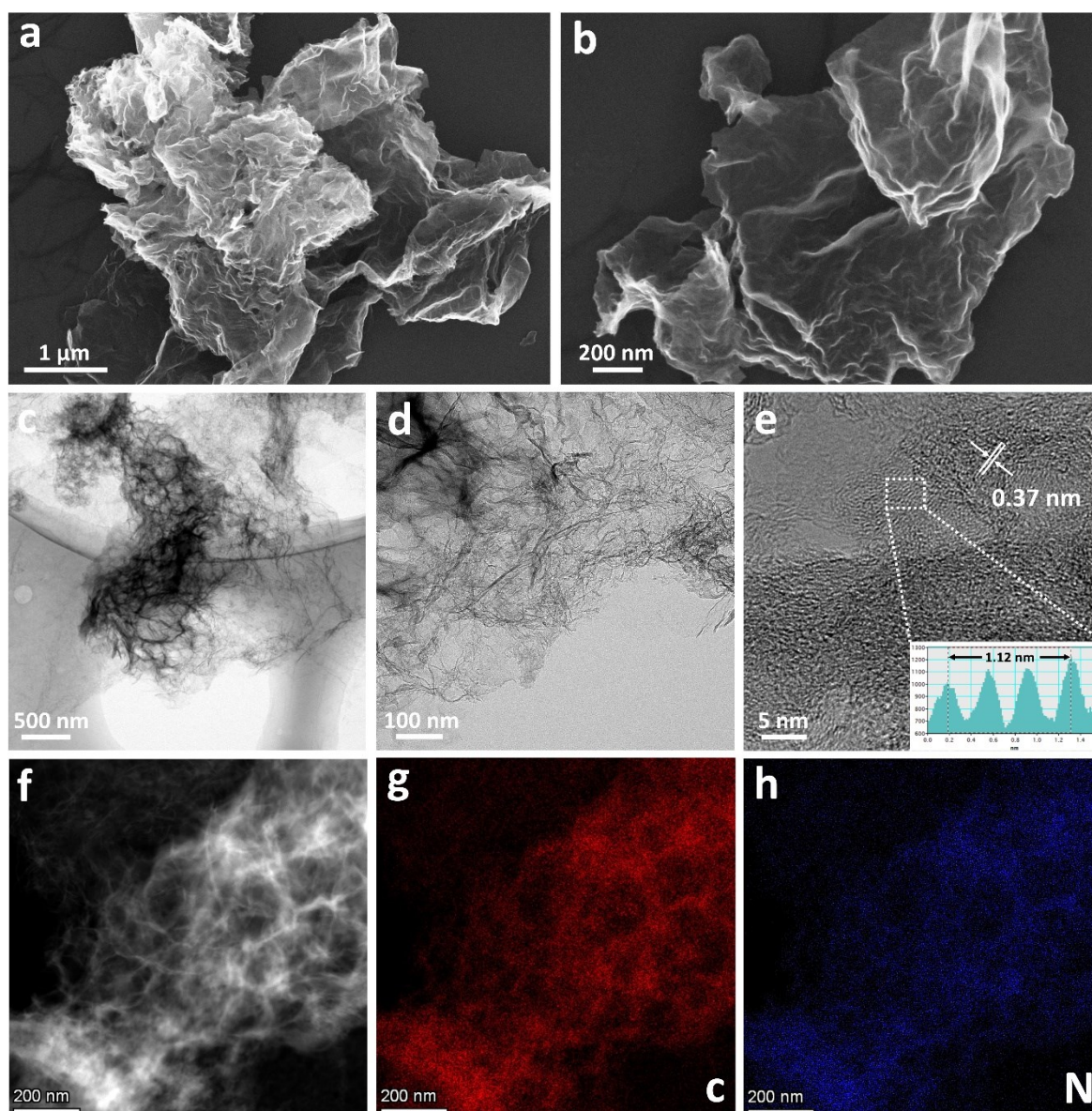
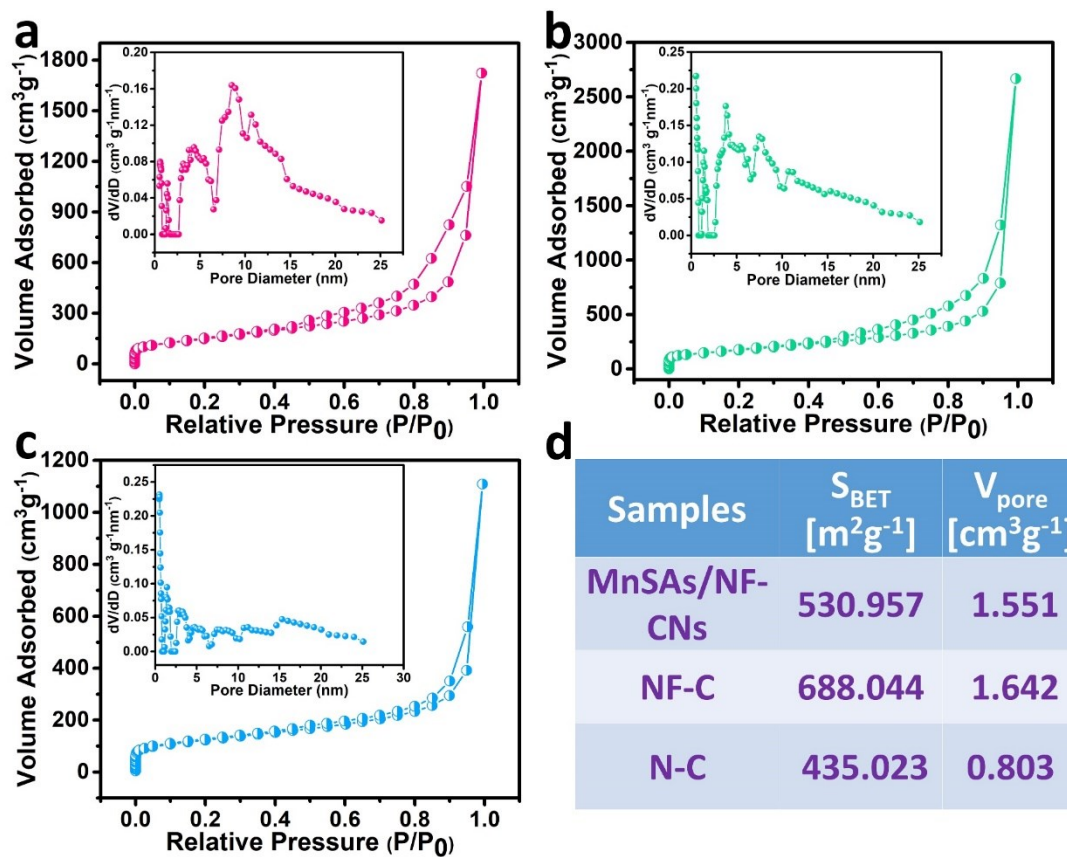**Figure S5**. (a, b) FESEM, (c, d) TEM, (e) HRTEM, (f-h) HAADF-STEM image and EDS elemental mappings of N-C.

Figure S6. (a-c) N_2 adsorption-desorption isotherm (inset is the DFT pore size distribution) of MnSAs/NF-CNs, NF-C and N-C, (d) Specific surface area and pore volume of all samples.

As shown in the pore size distribution, these porous carbon nanosheets are consist of micropores and mesopores. Although macropores can supply numerous fast ion-transport channels, much macropores will greatly reduce the packing density of porous carbon materials, resulting in the low volumetric capacitances of porous carbon electrodes for SIBs. Thus, the micropores and micropore-dominant 2D porous carbon nanosheet materials not only could decrease the ion diffusion distance and serve as reservoir for Na+ storage but also offer favorable volumetric capacitance.
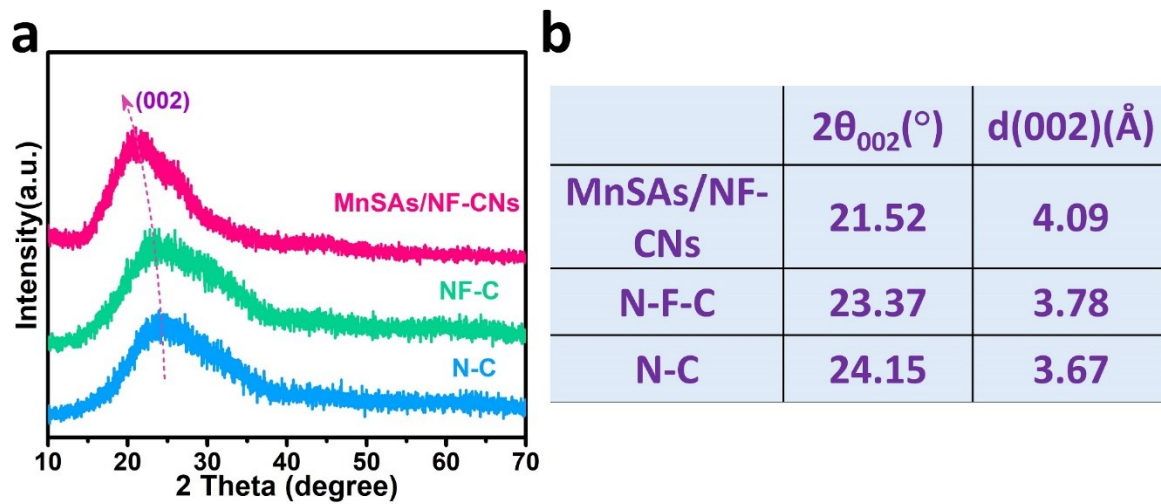
a — XRD pattern with peaks labeled (002) for MnSAs/NF-CNs, NF-C, and N-C; Intensity (a.u.) vs 2 Theta (degree), 10–70.

b

	$2\theta_{002}(°)$	$d(002)(\text{Å})$
MnSAs/NF-CNs	21.52	4.09
N-F-C	23.37	3.78
N-C	24.15	3.67

Figure S7. (a) XRD pattern and (b) corresponding interlayer distance calculated on Bragg equation of MnSAs/NF-CNs, NF-C and N-C.
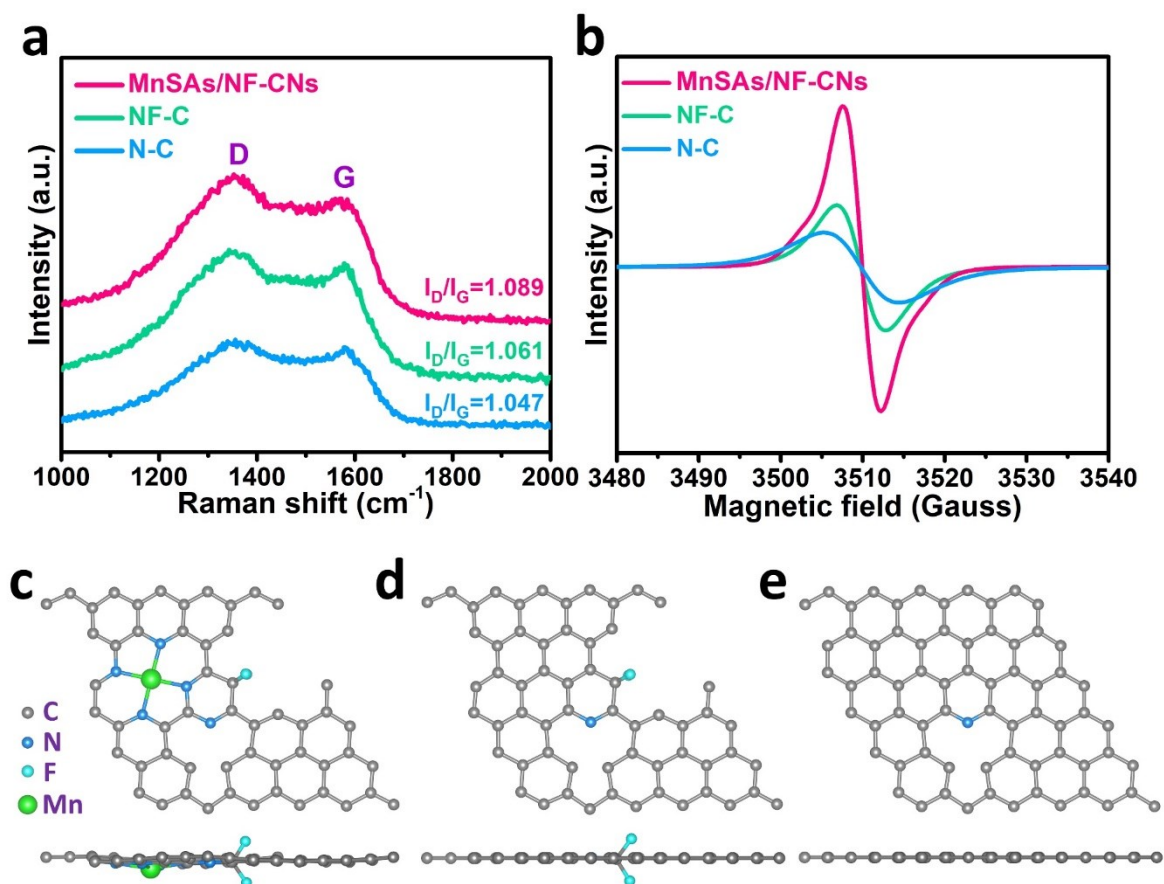
Figure S8. (a) Raman spectra and (b) Electron paramagnetic resonance (EPR) spectra of the MnSAs/NF-CNs, NF-C and N-C. Top and side view of the simulations structure of (c) MnSAs/NF-CNs, (d) NF-C and (e) N-C.
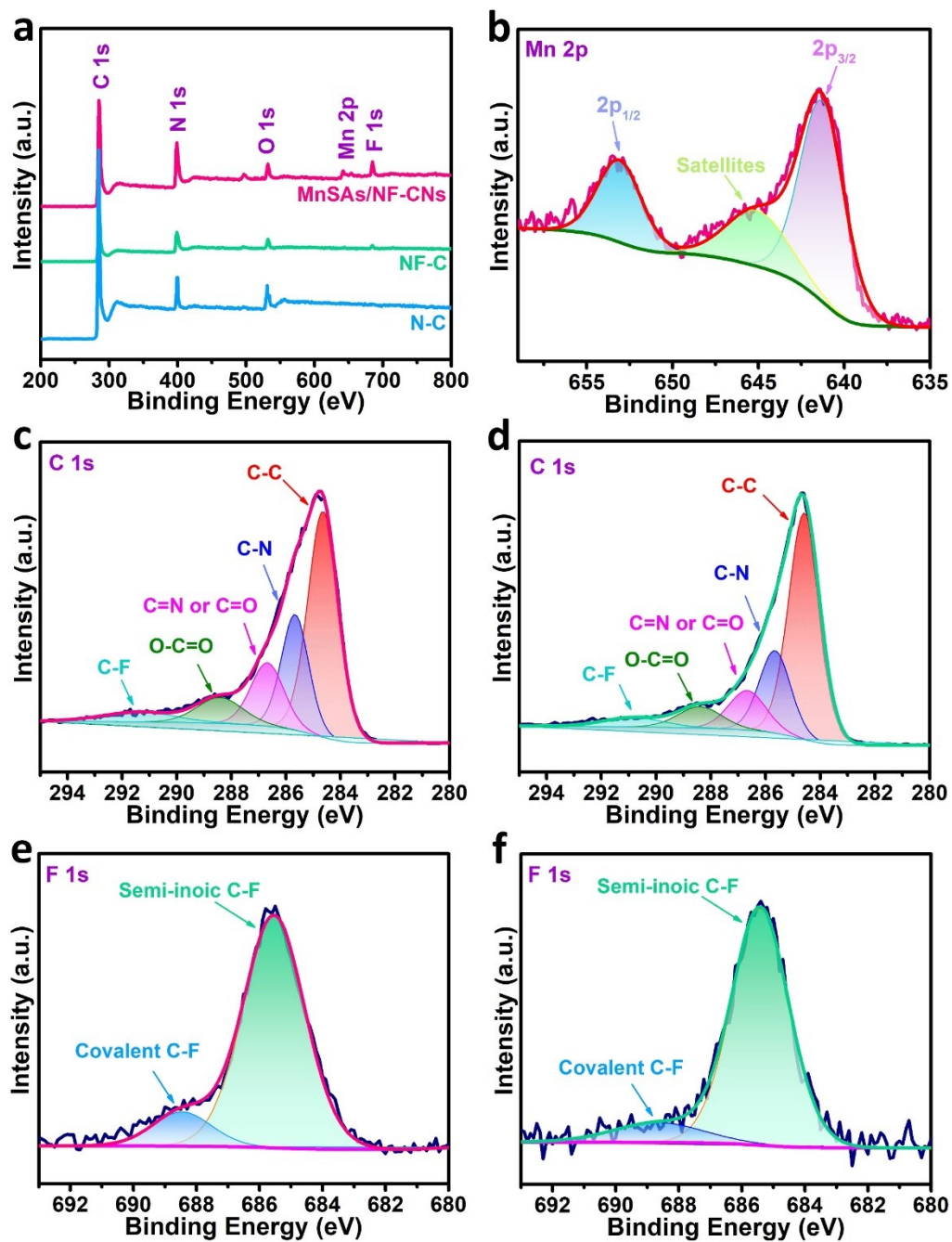
Figue S9. The survey XPS spectrum of MnSAs/NF-CNs, NF-C and N-C. (b) The high-resolution Mn 2p spectra of MnSAs/NF-CNs. The high-resolution C 1s spectra of (c) MnSAs/NF-CNs and (d) NF-C. The high-resolution F 1s spectra of (e) MnSAs/NF-CNs and (f) NF-C.
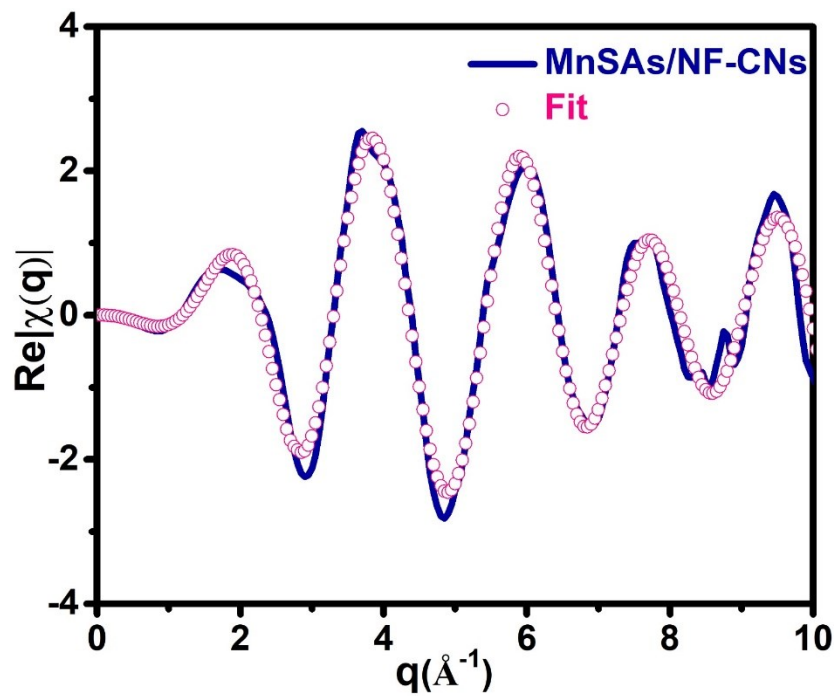
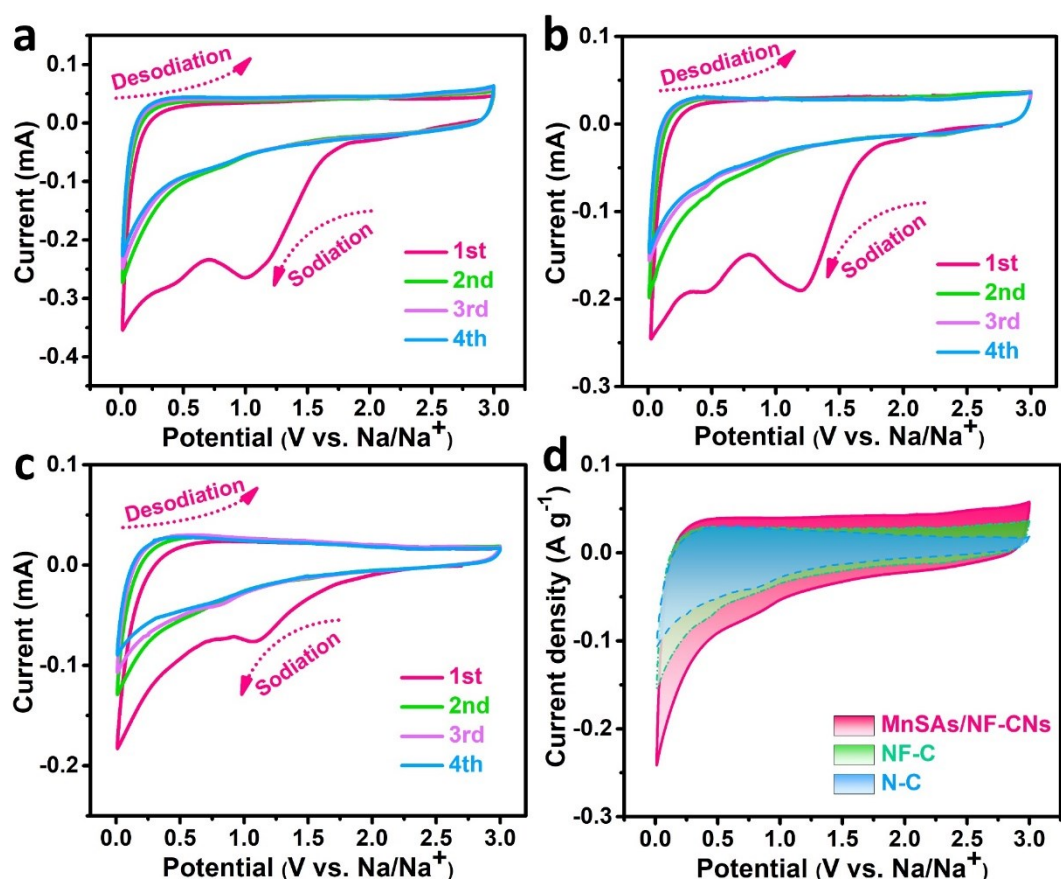**Figue S10.** The EXAFS fitting curves of MnSAs/NF-CNs in q space.

Figue S11. CV curves of the (a) MnSAs/NF-CNs, (b) NF-C and (c) N-C electrodes at a scan rate 0.1 mV s^{-1}. (d) CV curves of the MnSAs/NF-CNs, NF-C and N-C electrodes at a scan rate 0.1 mV s^{-1} for the 3rd cycle.

The broad cathodic peak at about 1.1 V and disappears in the following cycles of the MnSAs/NF-CNs, corresponding to the electrolyte decomposition, the solid-electrolyte interphase (SEI) formation, and some irreversible reactions between the Na ions and the surface functional groups. In the second cycle, a broad cathodic peak at 0.75 V and long cathodic slope, which could be ascribed to the Na$^+$ storage in defects or functional groups on the surface of carbon nanosheets (capacitive-controlled Na-storage). In addition, a sharp cathodic peak located at 0.01 V and a broad anodic peak at 0.25 V that are attributed to the intercalation and deintercalation of Na$^+$ between the carbon layers of MnSAs/NF-CNs (diffusion-controlled Na-storage), respectively. The smallest difference from the second cycle onward of CV curves suggests a stable electrochemical interaction of MnSAs/NF-CNs with Na ions.
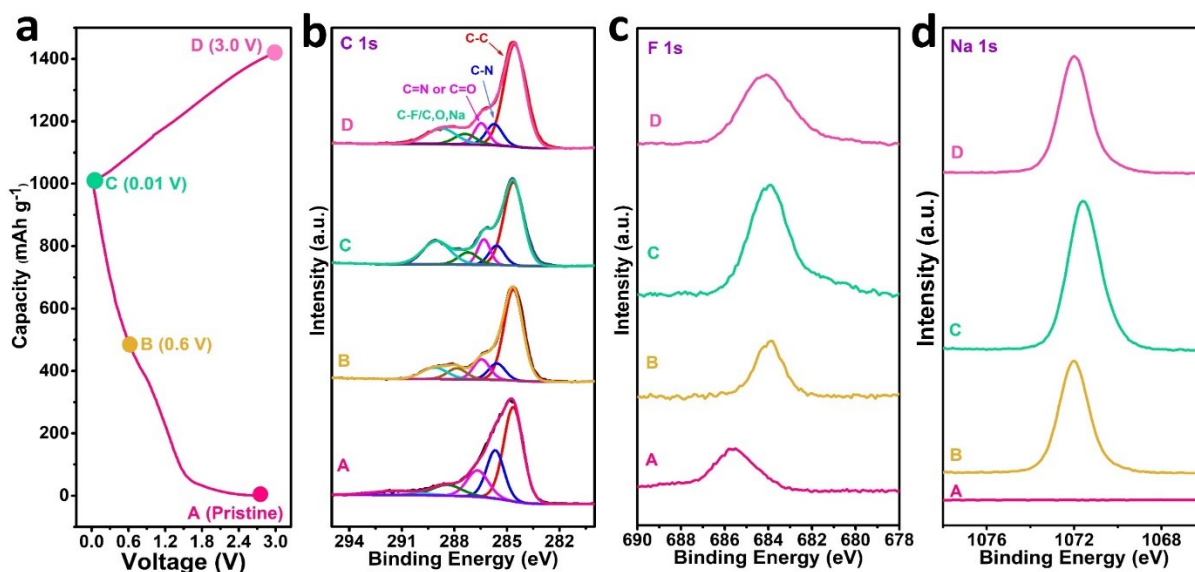
Figue S12. (a) Ex situ XPS profiles of MnSAs/NF-CNs in diferent states during the initial charge/discharge cycle and the corresponding voltage position of (b) C 1s, (c) F 1s, (d) Na 1s peaks.

Ex situ XPS measurements were carried out to elucidate the reaction mechanism of MnSAs/NF-CNs. In F 1s spectrum, the binding energy of the F 1s peak obviously shifted negative and the intensity increases with the uptake of Na^+ into the material, suggesting the intense interaction of Na^+ onto the active sites nearby F dopants and formation of NaF for SEI layer, which could effectively strengthen the stability of the electrode in the electrolyte. Simultaneously, the peaks at the high binding energy region of 287 - 291 eV in C 1s spectrum gradual increase during sodiation process, and then reduce but without vanish after fully desodiation state, which might be attributed to the growth of SEI layer and formation of some sodium-containing compounds, such as NaF, Na_2CO3, RCONa, R(O-C=O)Na, etc. (R represents various long-chain alkyl groups). In addition, the intensity of C-C bond in the C 1s spectrum gradually decreased after discharging to 0.01V and then increased after charging to 3 V, demonstrating the good reversibility of Na^+ insertion and extraction process. Moreover, the Na 1s peak moved in the lower binding energy direction upon discharge to 0.01 V, and reversibly moved in the higher binding energy direction in the subsequent charge process, further indicating reversible Na^+ insertion/extraction or reaction with surface functional groups.
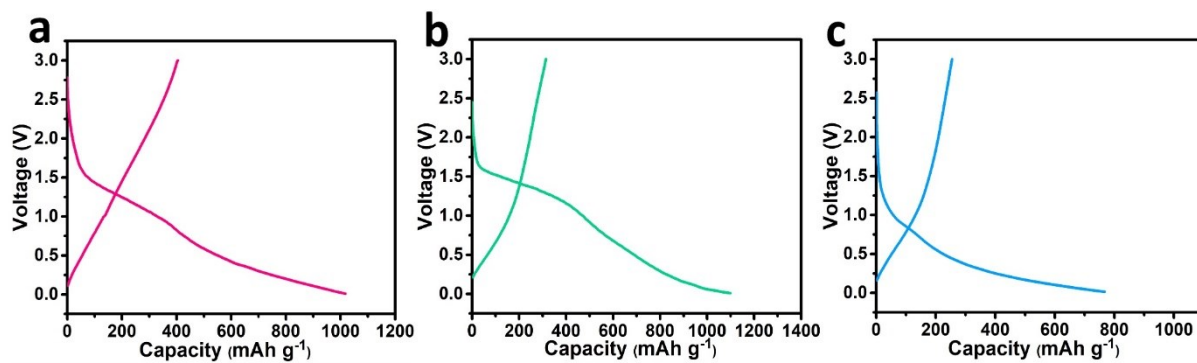
Figue S13. Initial charge-discharge profiles of (a) MnSAs/NF-CNs, (b) NF-C and (c) N-C electrodes at current density of 0.2 A g⁻¹. The results show that the MnSAs/NF-CNs delivers a higher initial reversible capacity of 405 mAh g⁻¹ than the NF-C (314 mAh g⁻¹) and N-C (253 mAh g⁻¹) electrodes.
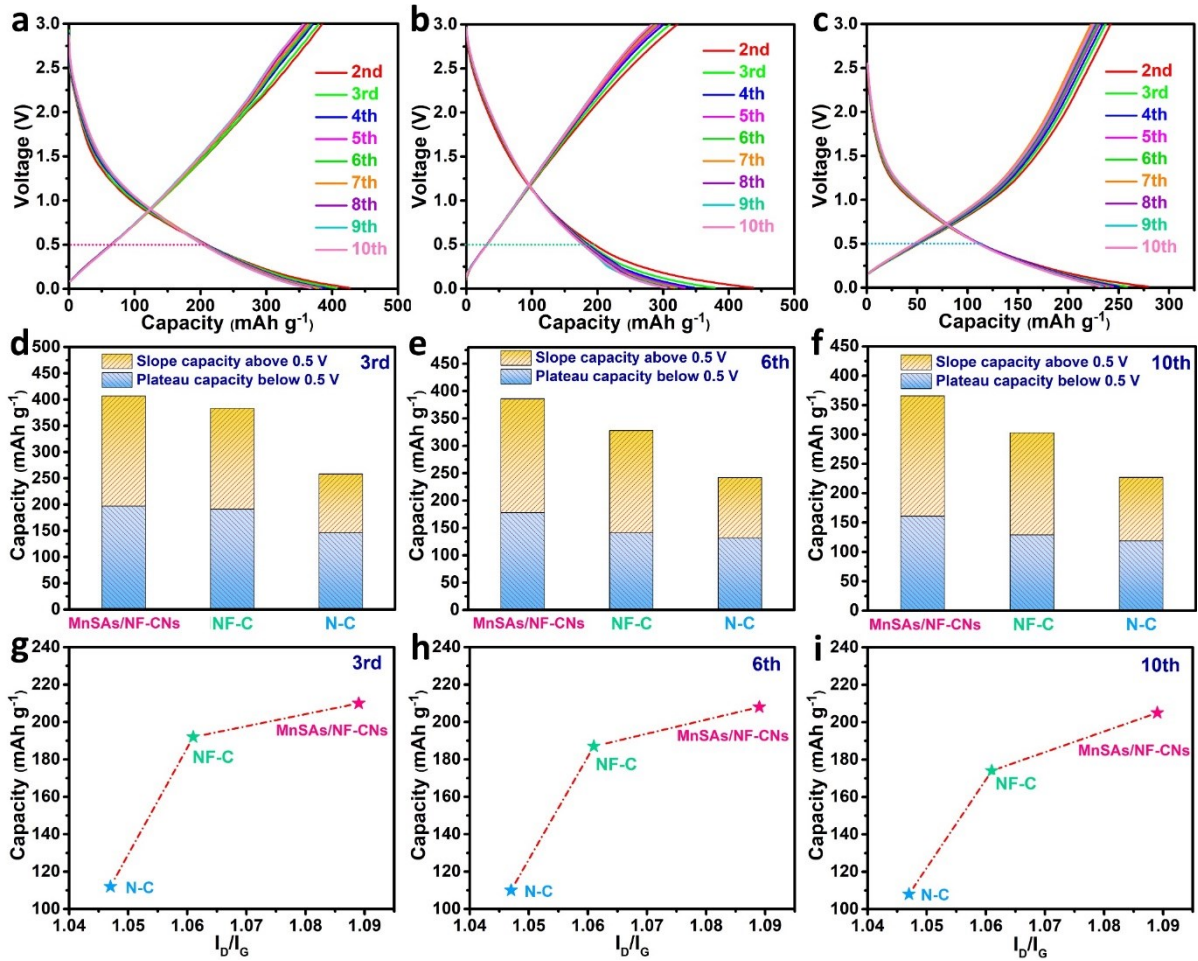
Figue S14. Charge-discharge profiles of (a) MnSAs/NF-CNs, (b) NF-C and (c) N-C electrodes the at current density of 0.2 A g⁻¹. (d-e) The capacity contribution at each stage of MnSAs/NF-CNs, NF-C and N-C. (g-i) Relation curves of the slope capacities and the ID/IG ratios.

We quantitatively surveyed the capacity assignment below and above the discharge voltage of 0.5 V to evaluate the practical application for full cell. According to the discharge curves, the MnSAs/NF-CNs displays the highest capacity among the three electrodes in the region of below and above 0.5 V. In addition, the slope shape of the GCD curves for these carbon electrodes is different from those of hard carbon materials with a low potential plateau close to 0 V, implying the capacity is mainly from the ion-trapping pore structures and abundant surface area sites for adsorption and intercalation of Na⁺ into the carbon layers. Moreover, the avoidance of low-potential plateau can relieve the danger of Na dendrite formation on the electrode surface during charging process and thus ensures higher safety. Note that the slope capacity decreases with the decrease of I_D/I_G at the high-potential sloping region, demonstrating the defects or surface functional groups induced by rich heteroatoms doping can provide abundant reactivity sites for the surface adsorption and thus increase the reversible capacity.
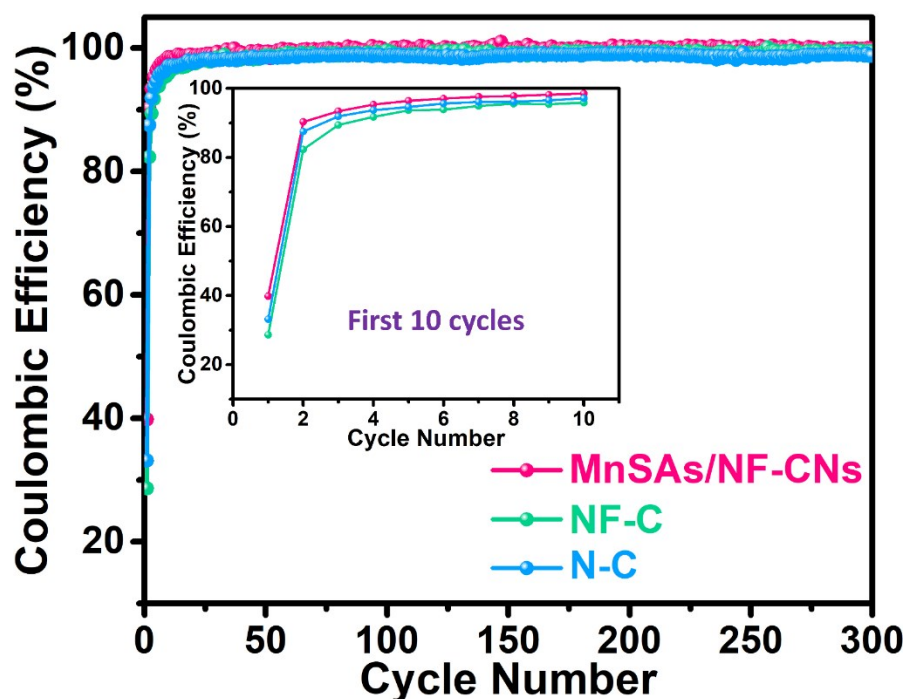
Figue S15. Coulombic dfficiency of the MnSAs/NF-CNs, NF-C and N-C electrodes for SIBs at a current density of 0.2 A g^{-1} for 300 cycles.

These carbon nanosheets all show a low initial Coulombic e☐ciency (ICE). Virtually, this initial irreversible capacity loss has often been reported in carbon based anodes. Nevertheless, the ICE of MnSAs/NF-CNs (39.8%) is much higher than those of NF-C (28.6%) and N-C (33.1%) electrodes as a result of the testified higher reversible capacity of MnSAs/NF-CNs in the first cycle. Moreover, the subsequent CE values of the MnSAs/NF-CNs quickly increase to 90.3% in the second cycle and approaches 100% from the 10th cycle. The results show that high specific surface area and well-developed pore structure of NF-C could consume a great deal of electrolyte to form SEI film, resulting in a relative low level of ICE compared to N-C and MnSAs/NF-CNs. Fortunately, the exist of atomically dispersed Mn in the MnSAs/NF-CNs electrode not only reduce the specific surface area and pore volume to avoid consume overmuch electrolyte, but also effectively regulate the local electronic structure and increase the electronic conductivity to deliver better reversibility, which contribute to form more effective SEI film on nanocarbon electrode and a remarkable electrochemical performance with a high and stable Coulombic efficiency.
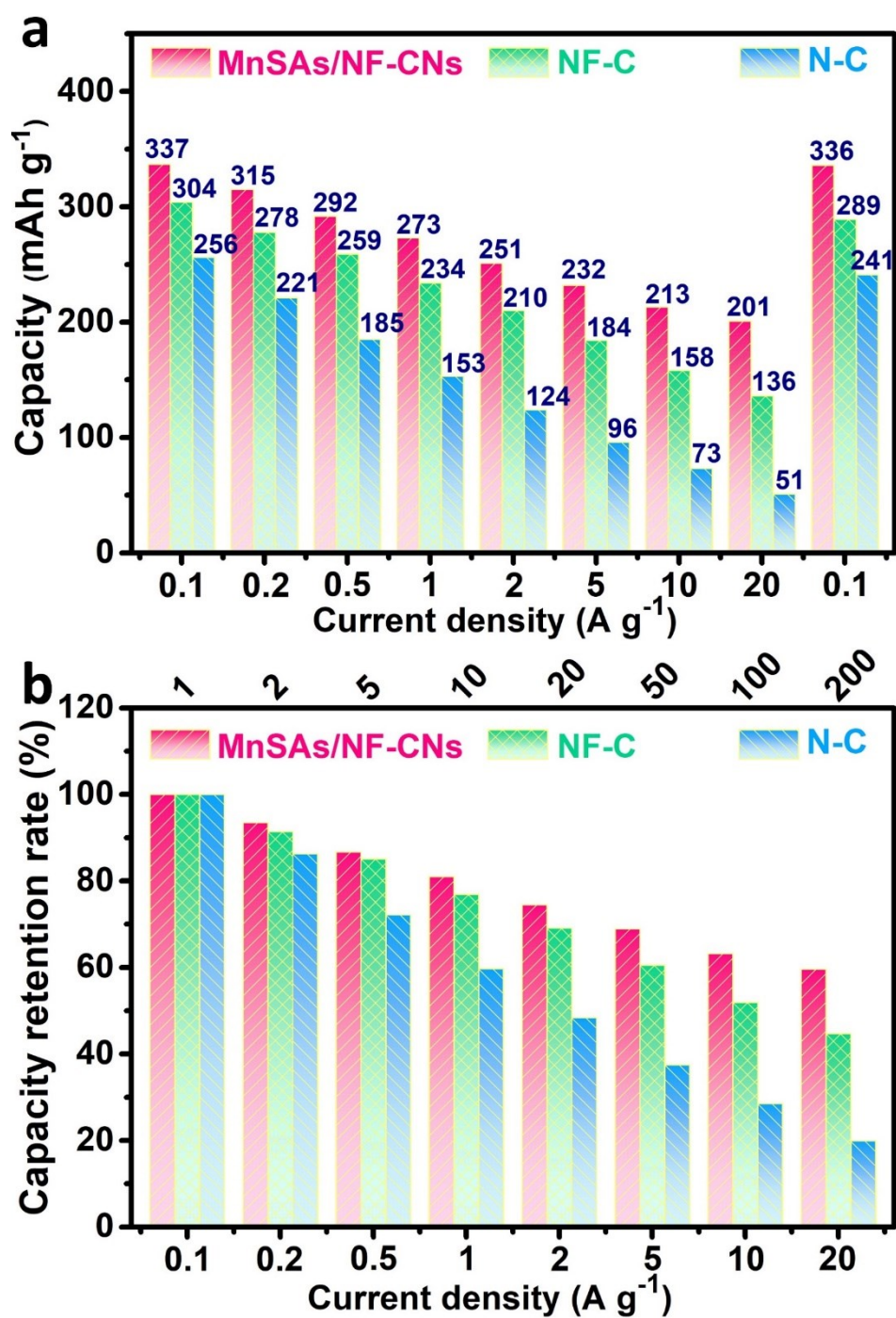
Figue S16. (a) The average capacities and (b) capacity retention rate of the three carbon electrodes at different current densities for SIBs corresponding to Figure 3d.
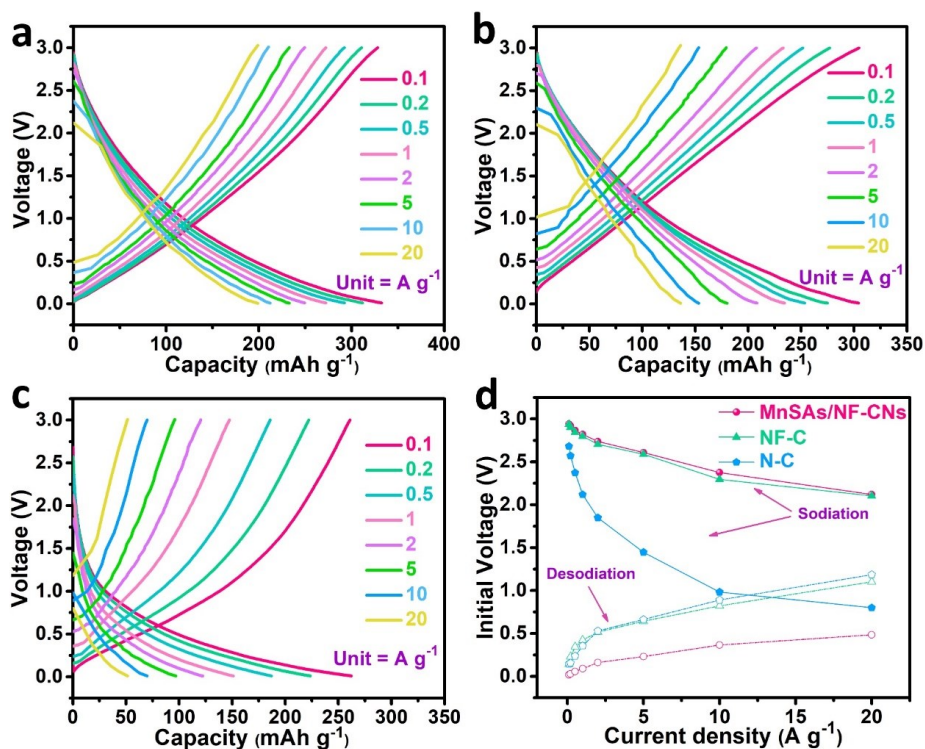
Figue S17. Charge-discharge profiles of the (a) MnSAs/NF-CNs, (b) NF-C and (c) N-C electrodes for SIBs at various current densities. (d) The initial voltages of sodiation/desodiation at different current density for these carbon electrodes.

As current densities increasing, the shape of GCD curves of MnSAs/NF-CNs is kept similar, revealing the perfect stability. Note that the MnSAs/NF-CNs still can keep a marvelous capacity retention rate of 59.6% even with 200-fold increase of current density, indicating the excellent rate performance. In addition, the smallest voltage hysteresis of MnSAs/NF-CNs at different current density among the three electrodes reveal the slightest electrode polarization. The excellent rate performance of the MnSAs/NF-CNs is attributed to three aspects: (1) the enlarged interlayer distance in the MnSAs/NF-CNs can mitigate the interlayer spacing change during cycling and accommodate more Na^+. (2) the ultrathin carbon nanosheets with hierarchical pore structure could offer integrated conductive network and rapid ion transfer length while increase the contact sites between electrode and electrolyte, resulting in fast Na^+ diffusion kinetics. (3) the existence of rich heteroatoms (atomically dispersed $Mn-N_4$, N and F co-dopants) in the porous carbon nanosheets not only enhance the affinity of the electrolyte and inhibit Na dendrite growth to some extent, but also providing more extra active sites for the reversible adsorption/desorption of Na^+, thereby improving the Na^+ storage capability.
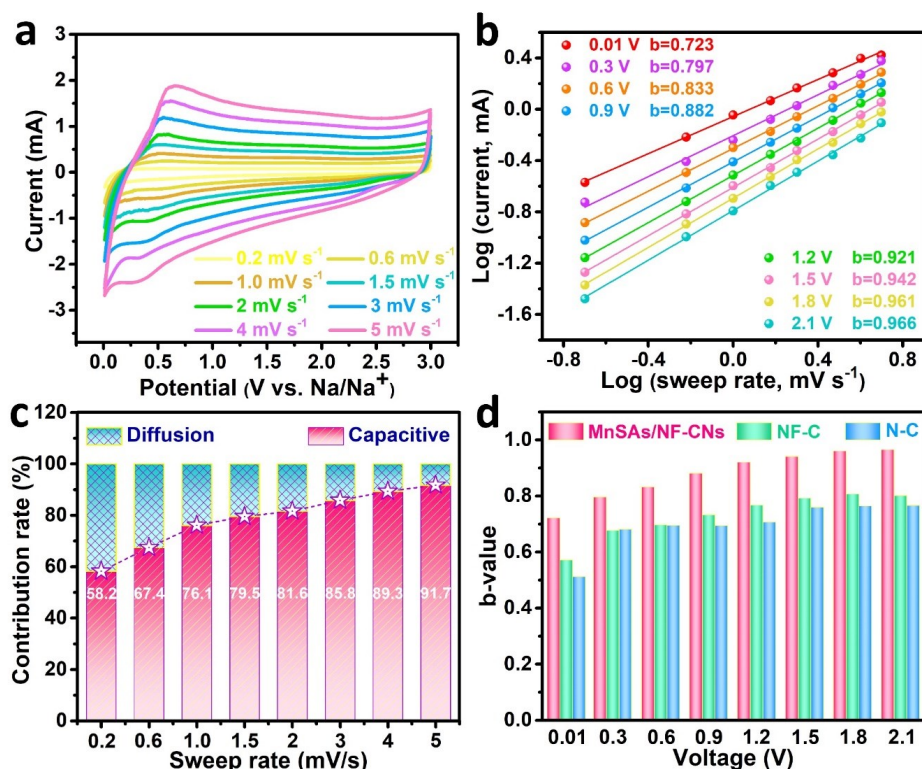
Figue S18. (a) CV curves at various scan rates from 0.2 to 5.0 mV s^{-1}, (b) Linear relationships between logarithm currents and logarithm sweep rate and (c) normalized contribution ratio of capacitive and diffusion at different scan rates. (d) b values of the MnSAs/NF-CNs, NF-C and N-C at different voltage for cathodic scans.

Inspired by the high Na$^+$ storage capacity and high-rate capability of MnSAs/NF-CNs anode, the in-depth kinetic analyses were conducted based on CV tests with multiple scan rates. At the low potentials (0.01 and 0.3 V), the calculated b values of MnSAs/NF-CNs are close to 0.75 and higher than NF-C and N-C, revealing that the capacity contributions are controlled by both faradaic intercalation process driven by ampliative interlayer distance and surface active sites-induced capacitive behavior. At the high potentials (especially exceed 1.0 V), the b values are greater than 0.9 only for MnSAs/NF-CNs, indicating that the Na$^+$ storage is governed by capacitive effect process due to ample heteroatoms-codoping, and thus resulting in the high-rate property. In addition, the pseudocapacitive contribution of the MnSAs/NF-CNs increased gradually with the increasing scan rates and reaches 91.7% at a high scan rate of 5 mV s^{-1}, larger than that of NF-C and N-C at each scan rate, demonstrating the atomically dispersed Mn facilitate better surface-redox reaction rate of the MnSAs/NF-CNs electrode and benefit its faster reaction kinetics.
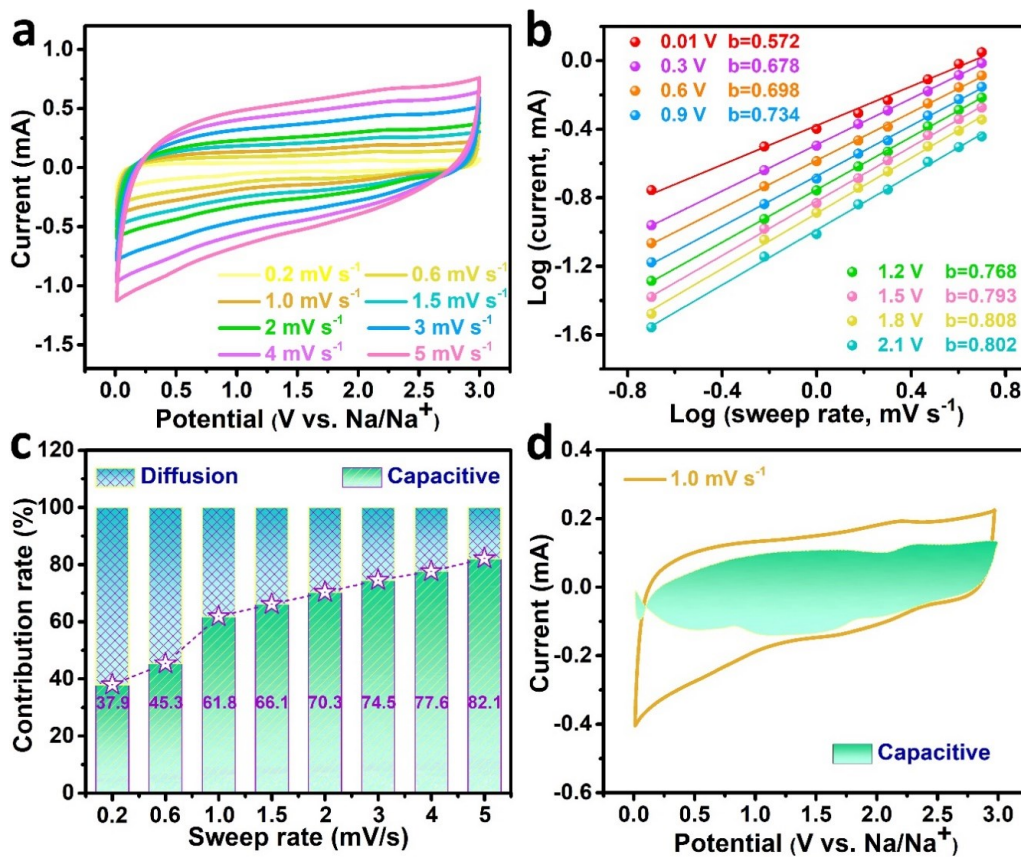
25

Figue S19. (a) CV curves at various scan rates from 0.2 to 5.0 mV s^{-1}, (b) Linear relationships between logarithm currents and logarithm sweep rate, (c) normalized contribution ratio of capacitive and di□usion at di□erent scan rates and (d) capacitive contribution at 1.0 mV s^{-1} of NF-C electrode.
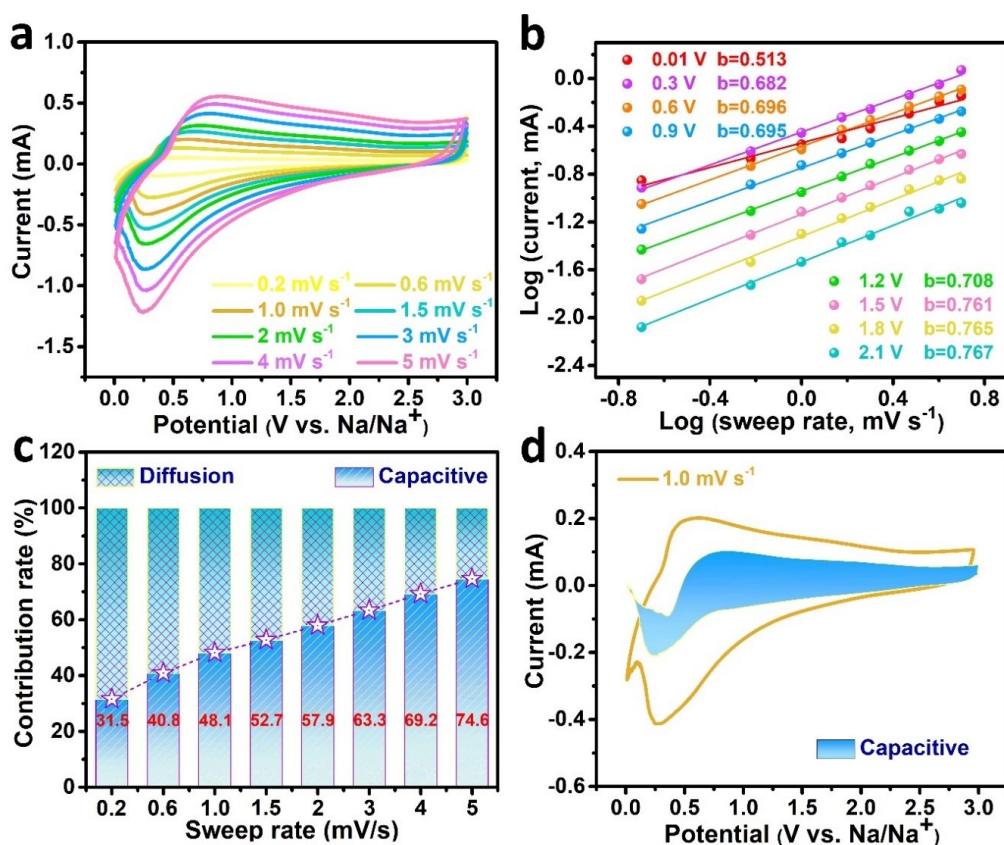
Figue S20. (a) CV curves at various scan rates from 0.2 to 5.0 mV s⁻¹, (b) Linear relationships between logarithm currents and logarithm sweep rate, (c) normalized contribution ratio of capacitive and di□usion at di□erent scan rates and (d) capacitive contribution at 1.0 mV s⁻¹ of N-C electrode.
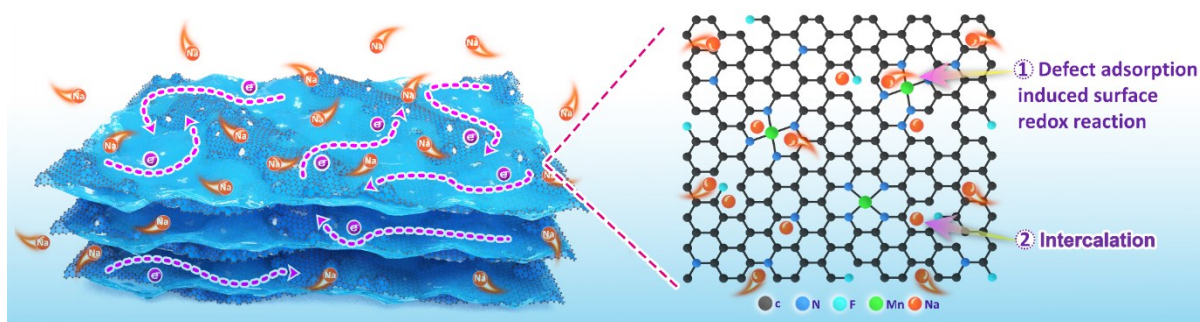
Figue S21. Schematic illustration of Na storage mechanisms for the MnSAs/NF-CNs electrode.

The possible sodium storage mechanism is proposed according to the sloping discharge profiles and CV curves analysis. The discharge profiles of three carbon nanosheets are divided into two stages: (1) the high-potential slope starts from the beginning of discharge and ends on a capacitive region (obtained from the b value), Na^+ mainly adsorb on the surface defect sites and storage at surface functional groups generated by rich heteroatoms codoping, which is on behalf of the surface-dominated capacity. (2) Then Na^+ intercalation/deintercalation between the disordered carbon interlayer is occurred at the low potentials plateau, showing diffusion-controlled processes and slow kinetics. Thus, a "defect adsorption-intercalation" mechanism is schematically illustrated in Figure S21 for the MnSAs/NF-CNs electrode.

Compared with the reported carbon anode, the capacity of the MnSAs/NF-CNs is extraordinary high, which is higher than the theoretical value of graphite (279 mA h^{-1}). Two reasons can account for this particular phenomenon: (1) the Na^+ storage mechanism of amorphous MnSAs/NF-CNs is much different from well-crystallized graphite. The narrow interlayer spacing of the layered graphite severely limited the intercalation number of the large size of Na^+. The amorphous carbon grain with enlarged interlayer distance in a short range, which would be highly favorable for accommodating more Na^+ and adapting the interlayer distance variation during cycling. (2) The MnSAs/NF-CNs not only possesses larger nominal interlayer distance but also furnish abundant intrinsic defects and extra active sites on the surface and edge for Na^+ storage owing to the existence of numerous Mn single atoms, N, F co-dopants and porous structure. According to the "defect adsorption-intercalation" mechanism, the Na^+ can adsorb on the surface of porous carbon nanosheets and edge active sites first, and subsequent insert into the carbon layers. Therefore, a part of the capacity can be generated from a good deal of Na^+ adsorbs on the reaction active sites of edges and defects in MnSAs/NF-CNs.
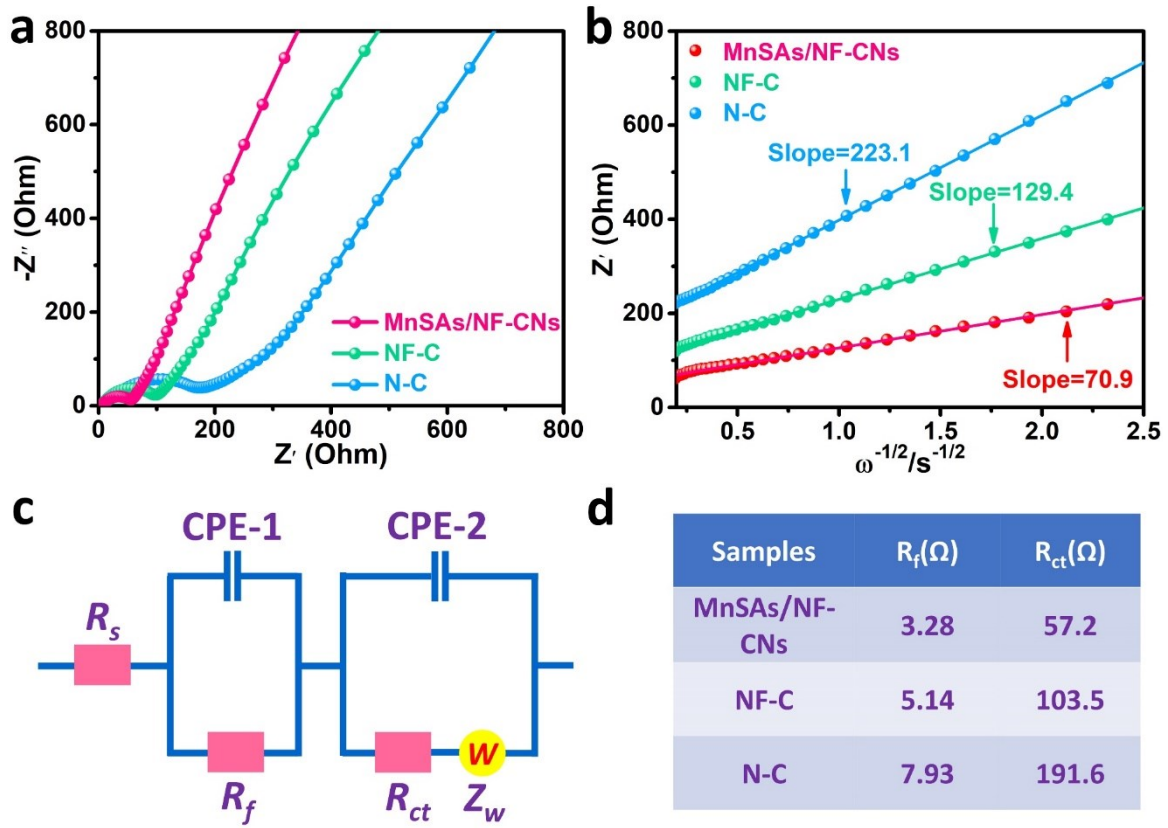
Figue S22. (a) Electrochemical impedance spectra (EIS) of the MnSAs/NF-CNs, NF-C and N-C electrodes after cycling at 0.2 A g^{-1} and (b) linear fits of the Z` versus $\omega^{-1/2}$ ($\omega = 2\pi f$) in the low-frequency region. (c) the corresponding equivalent circuit model. (d) The EIS fitting parameters of MnSAs/NF-CNs, NF-C and N-C electrodes.

Electrochemical impedance spectroscope simulation: the impedance data is simulated by electric equivalent circuit (Figure S22c), where R_f and CPE-1 are the electrolyte resistance and double-layer capacitance, R_{ct} and CPE-2 represent the charge-transfer resistance at the interfaces and capacitance of the surface film, Z_w is the Warburg impedance associated with the di□usion of Na$^+$ in the carbon electrode. The semicircle has been differentiated to the SEI film and contact resistance at high frequencies and a R_{ct} in the middle-frequency, while the linear increase in the low-frequency range can be related to Z_w. In the Nyquist plots, the MnSAs/NF-CNs electrode shows a lower R_{ct}, indicating higher conductivity and faster charge-transfer kinetics than those of NF-C and N-C. Moreover, the MnSAs/NF-CNs electrode shows the largest slope of straight line among these samples, suggesting the smallest Warburg impedance that corresponds to highest Na$^+$ diffusion ability inside the electrode.
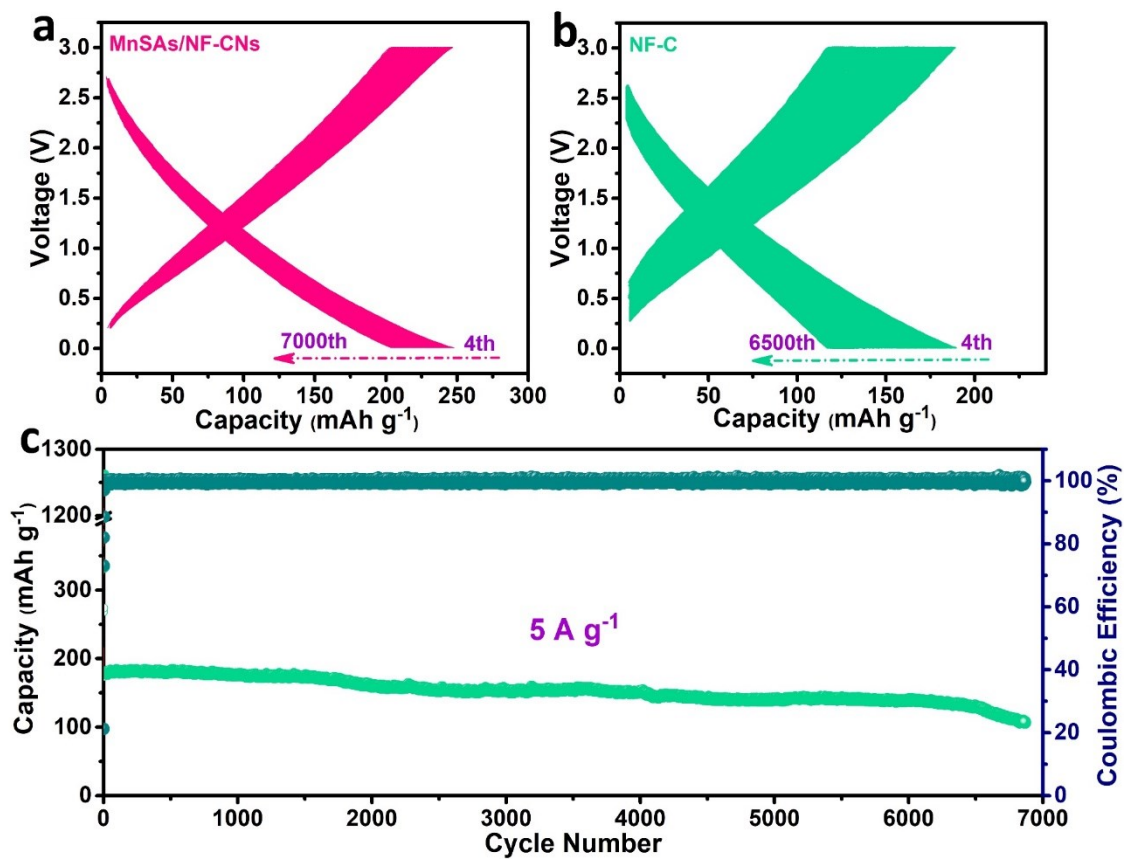
Figue S23. Charge-discharge profiles of the (a) MnSAs/NF-CNs and (b) NF-C. (c) The cycling performance of NF-C at a high current rate of 5 A g^{-1}.
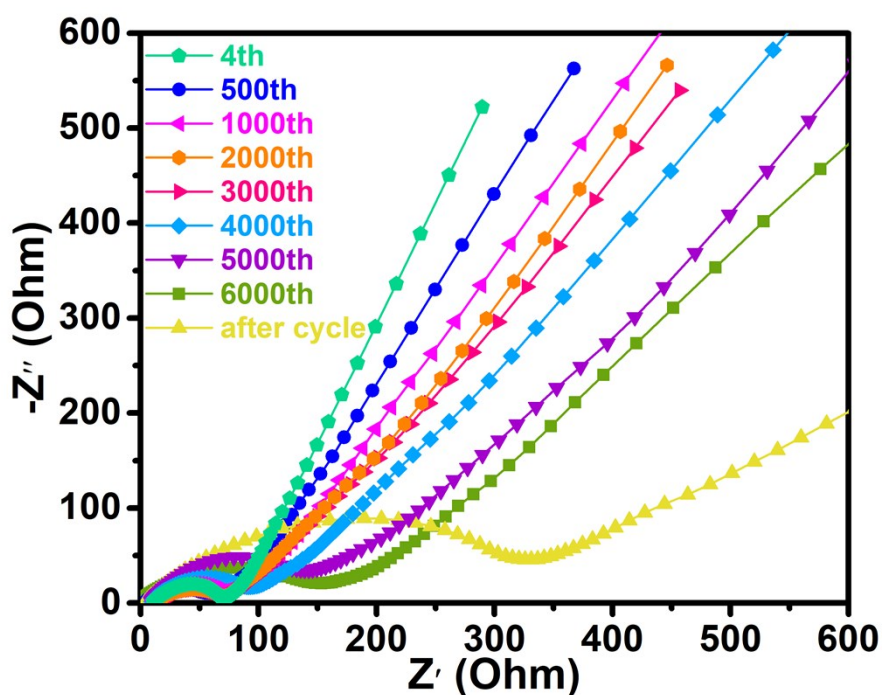
Figue S24. EIS spectra of NF-C electrode after different charge-discharge cycles at a current density of 5.0 A g^{-1}.

A stable electrode/electrolyte interface and a path suitable for fast Na^+ transport is critical for excellent electrochemical performance. The diameter of the semicircle for the NF-C electrode keeps increasing as cycling continues, while the slope of straight line decreased gradually, indicating the continuous increase of R_{ct} and decrease in diffusion coefficients of Na^+ as well as repeated growth of SEI after the repeated Na^+ insertion/extraction process. Thus, the NF-C electrode displays worse stability of electrode/electrolyte interface, leading to fast capacity fading and cell failure. In contrast, Nyquist plots of the EIS spectra for MnSAs/NF-CNs electrode exhibit the same shape including the semicircle and slope at different cycles, and the semicircles are much smaller than NF-C, reflecting a faster charge transfer process in MnSAs/NF-CNs electrode. This phenomenon demonstrates that Mn single atoms and N, F co-doping, enlarged carbon layer spacing, and porous structure in the MnSAs/NF-CNs can not only afford more efficient storage sites for Na^+ to increase the reversible capacity, but also provide optimized Na^+ diffusion paths to facilitate the charge transfer, thus leading to the formation of a stable electrode/electrolyte interface and guarantee the structural integrity.
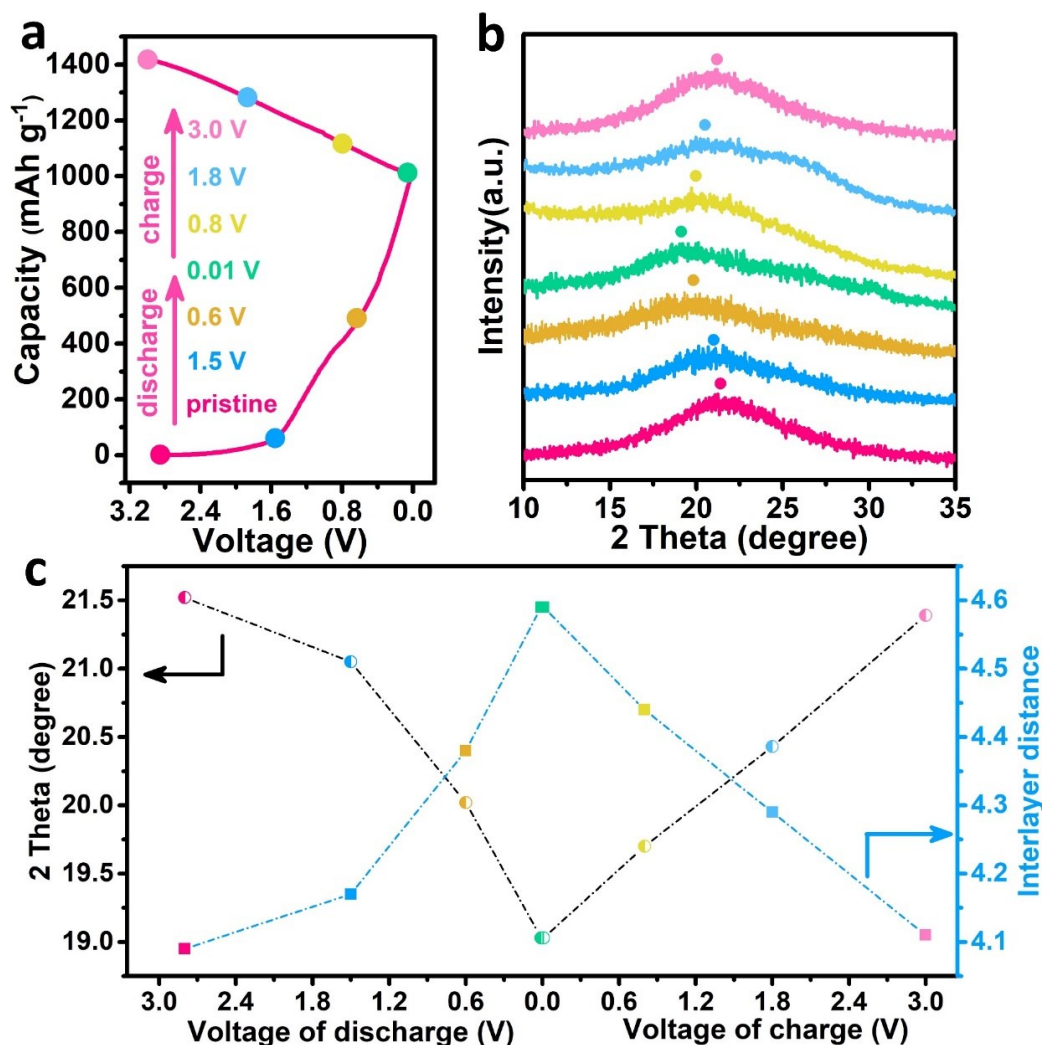
Figue S25. (a) Voltage profiles of the MnSAs/NF-CNs electrode in the first cycle at 0.2 A g-1. (b) Ex-situ XRD patterns and (c) illustration of the corresponding peak location and interlayer distance at different stages during the initial charge/discharge process of MnSAs/NF-CNs.

Upon the sodiation/desodiation process, the (002) diffraction peak shifted from 21.52°, 21.05°, 20.02°, 19.04°, 19.7°, 20.43° and 21.39° at various stages of 2.8, 1.5, 0.5, 0.01, 0.8, 1.8, 3.0 V, corresponding to the interlayer distances of 0.409, 0.417, 0.438, 0.459, 0.444, 0.429 and 0.411 nm , respectively. Ex situ XRD of MnSAs/NF-CNs does not present a obvious shift of the (002) peak during discharging at high-potential region, maybe due to adsorption of Na^+ on the surface of carbon nanosheets instead of intercalation. Although the interlayer distance is expanded by the larger sizes of Na ions insertion at full sodiation stage, the rate of volume expansion is only 12.2%, indicating the enlarged interlayer spacing of MnSAs/NF-CNs could accommodate the insertion and extraction of Na^+. Moreover, the diffraction peak is recovered to original position after deintercalation to 3.0 V, demonstrating the excellent structure reversibility of MnSAs/NF-CNs.
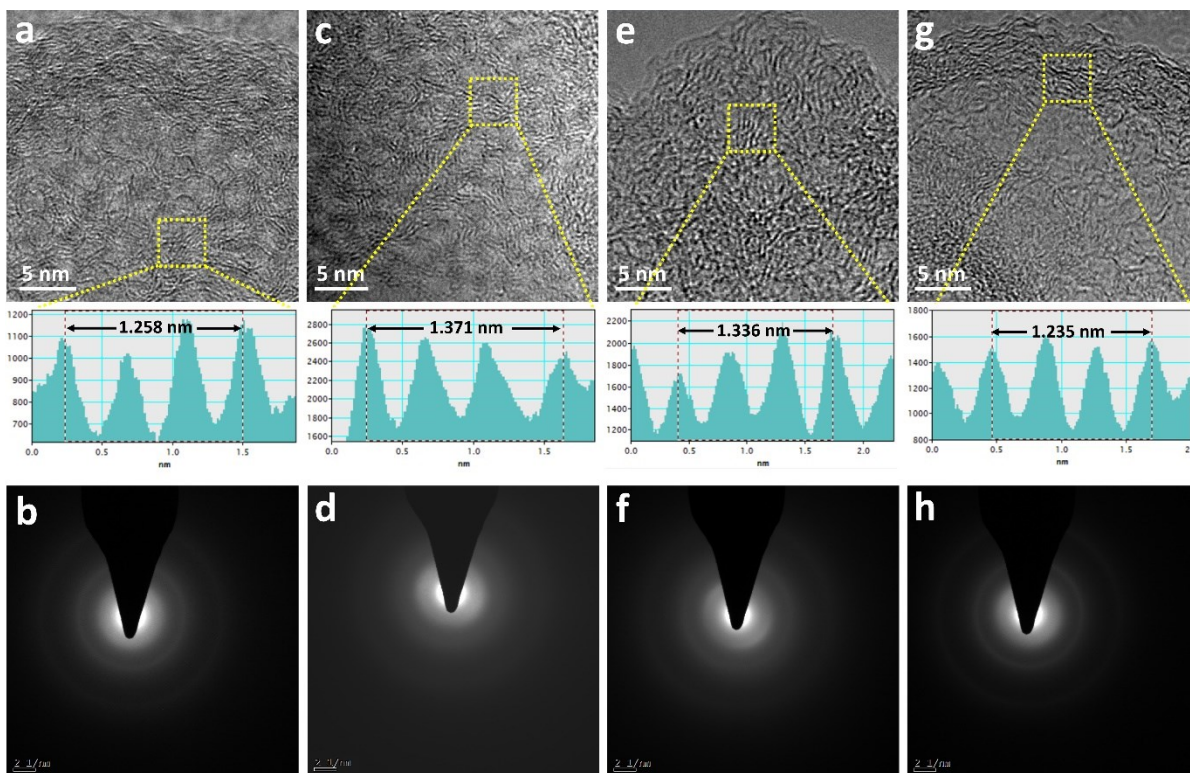
Figue S26. Ex-situ HRTEM images of the MnSAs/NF-CNs electrode at different discharge/charge states: (a-b) discharge to 1.5 V, (c-d) discharge to 0.01V, (e-f) charge to 0.8 V and (g-h) charge to 3.0 V.

The Na ions insertion reaction in the MnSAs/NF-CNs electrode was directly visualized by HRTEM measurement. The average interlayer distance mild increases to about 0.419 nm after discharge to 1.5 V, attributed to the Na^+ adsorb onto the surface defect sites and partly intercalate to the edge of graphitic-like domains. After full sodiation at 0.01 V, the interlayer distance expands to a higher value (0.457 nm). The HAADF-STEM image and EDS mapping results display that C, N, F, Mn and Na distributed homogeneously over the carbon nanosheets, further testifying the successful intercalation of Na^+ into the MnSAs/NF-CNs electrode. Subsequently, interlayer distance gradually decreased to 0.411 nm as the charge potential returned to 3.0 V, being consistent with the ex-XRD results. The selected area electron diffraction (SAED) patterns confirmed that the atomically dispersed Mn remain amorphous Mn species during the sodiation/desodiation prosess. Despite the larger sizes of Na^+ insertion, the MnSAs/NF-CNs electrode can offer an enlarged carbon interlayer distance and robust chemical bonds to accommodate the volume variation for the insertion/extraction of Na^+, thus resulting in the distinguished structure stability and long-term cycling lifetime.
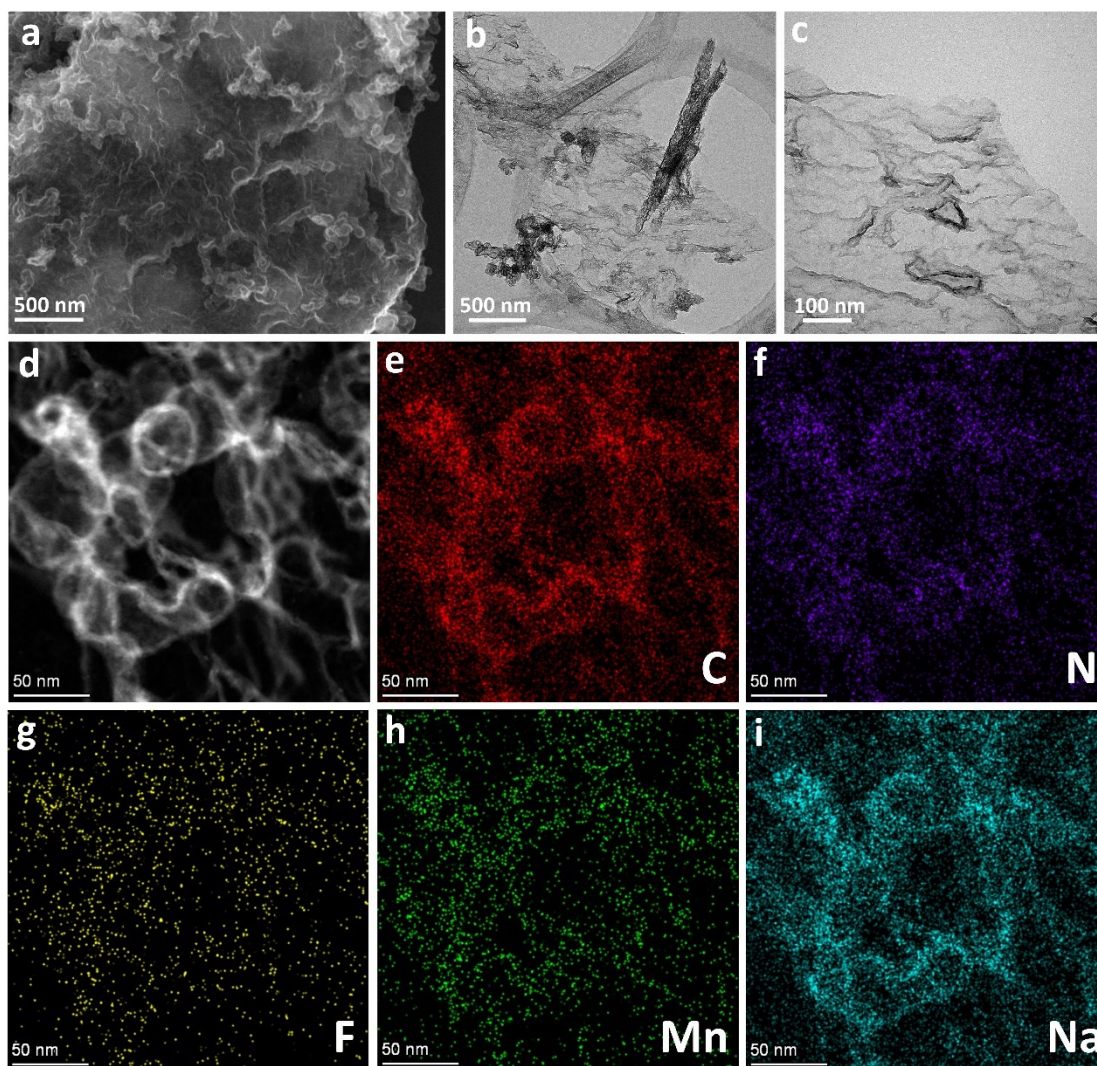
Figue S27. (a-c) FESEM and TEM images, (d-i) HAADF-STEM image and EDS mappings of the MnSAs/NF-CNs electrode after full sodiation.
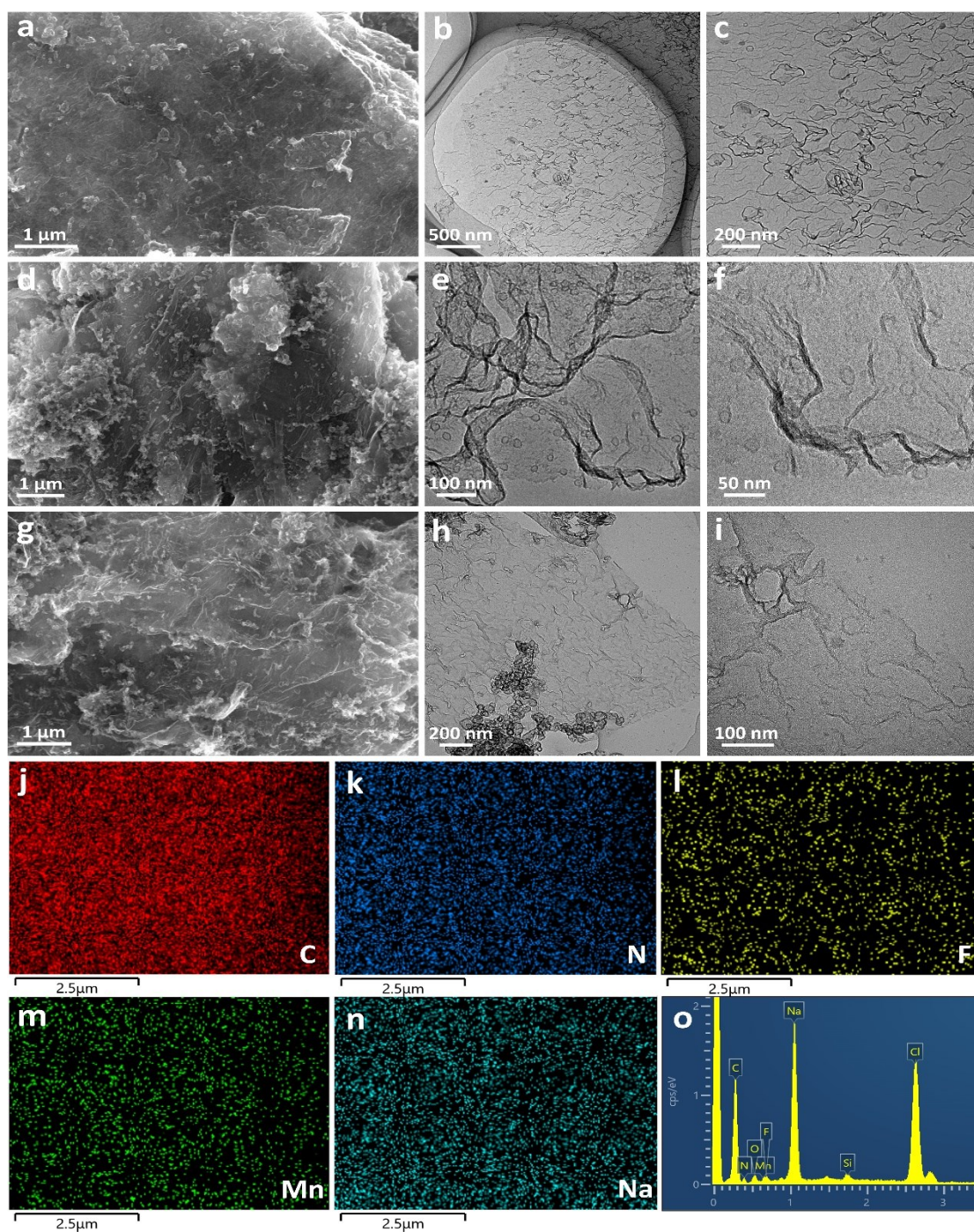
Figue S28. The FESEM and TEM images for the MnSAs/NF-CNs at 5 A g^{-1} after (a-c) 100 th, (d-f) 1000 th, (g-i) 7000 th. (j-n) The corresponding elemental mappings and (o) EDS spectra of the MnSAs/NF-CNs after 7000 cycle at 5 A g^{-1}.
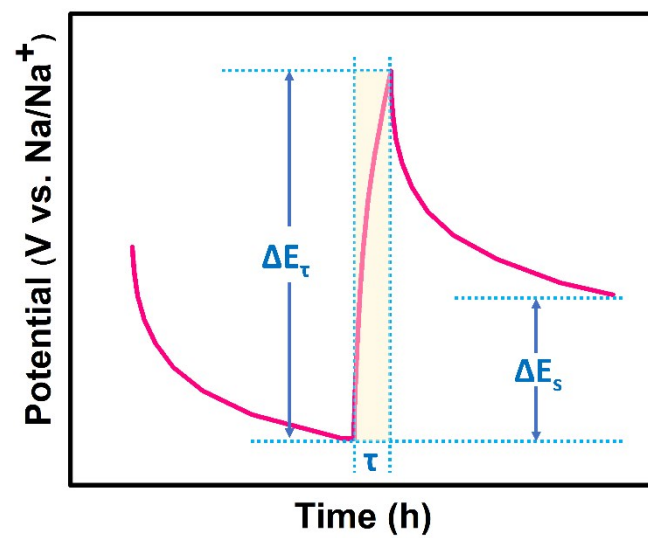
Figue S29. Current step diagram of parameter determination for GITT measurement.
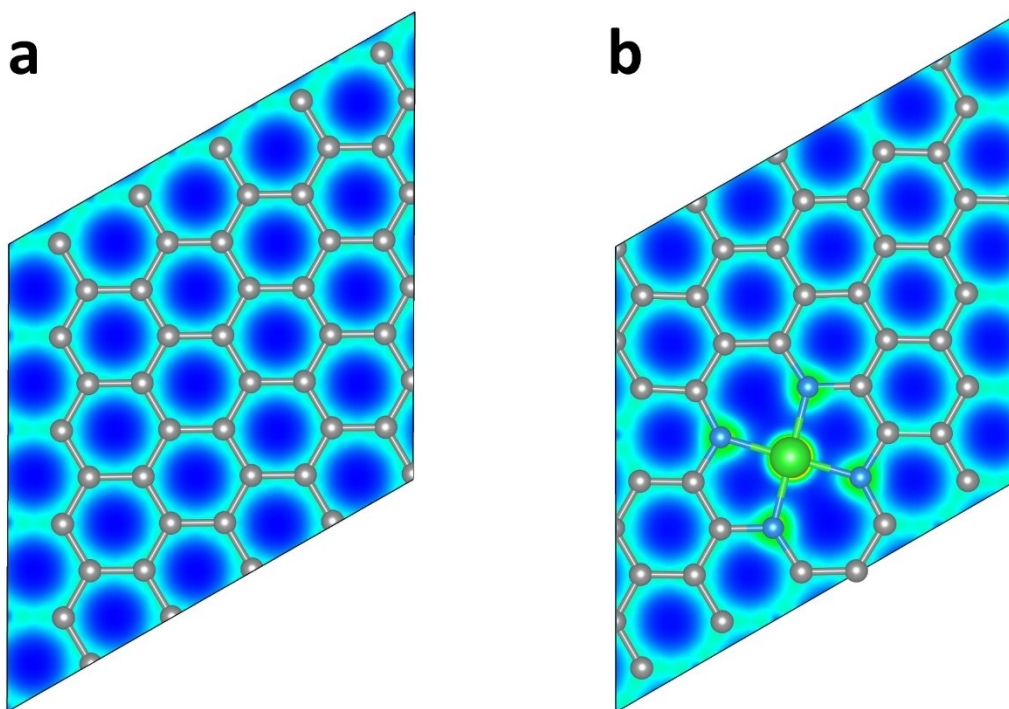
Figue S30. Top views of optimized (a) pure carbon and (b) MnN_4-C, and the isosurfaces of the cross-sectional charge density.

Figue S31. (a) Top and side illustration of simulations for a single Na ion adsorbed on the pure carbon and the corresponding ΔEa. (b) Calculated charge density differences of Na ion adsorbed on the pure carbon structure.

Figue S32. (a) Top and side illustration of simulations for a single Na ion adsorbed on the N-C and the corresponding ΔEa. (b) Calculated charge density differences of Na ion adsorbed on the N-C structure.

ΔE_a = -3.96 eV

Figue S33. (a) Top and side illustration of simulations for a single Na ion adsorbed on the NF-C and the corresponding ΔEa. (b) Calculated charge density differences of Na ion adsorbed on the NF-C structure. The high electronegativity of F atom in the NF-C provides a stronger adsorption energy (-3.96 eV) for Na^+ than N-C (-2.33 eV) and pure carbon (-0.28 eV) while the protrusions structure caused by doped F conduces to expand the interlayer spacing of the carbon layer.

ΔE_a = -1.55 eV ΔE_a = -2.19 eV ΔE_a = -3.91 eV
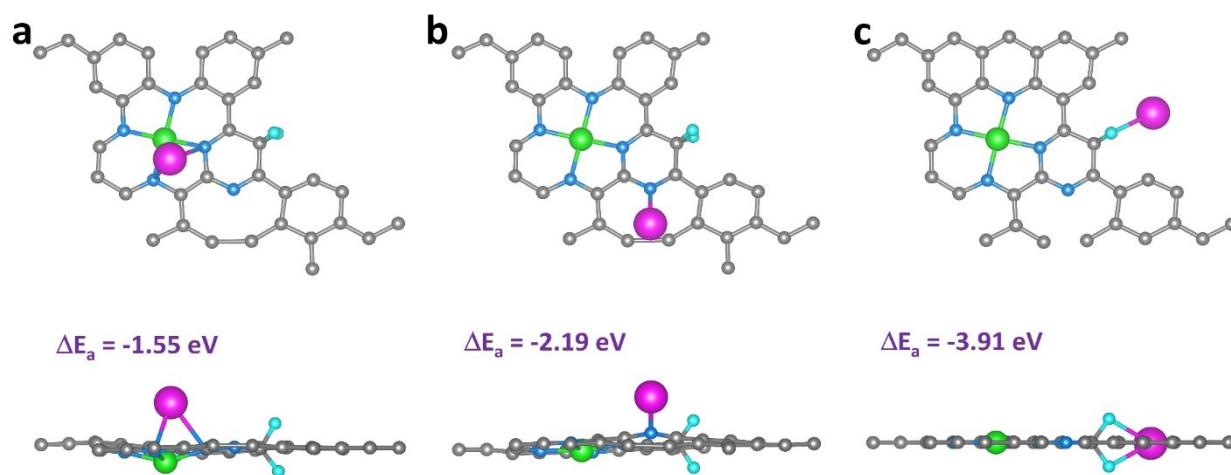
Figue S34. Top and side illustration of simulations for a single Na ion adsorbed on the different active sites of (a) Mn, (b) N and (c) F of MnSAs/NF-CNs electrode and their corresponding ΔEa.
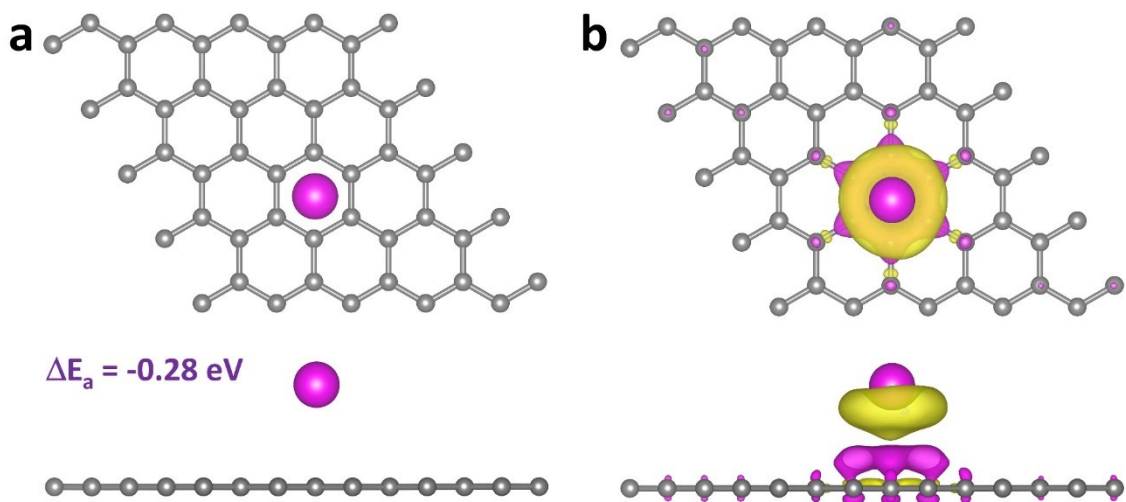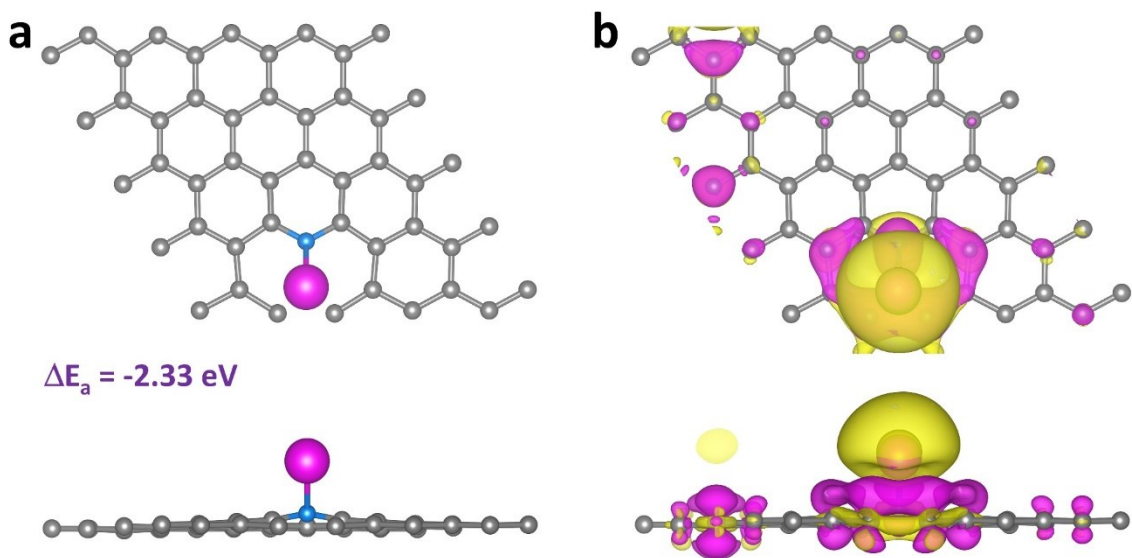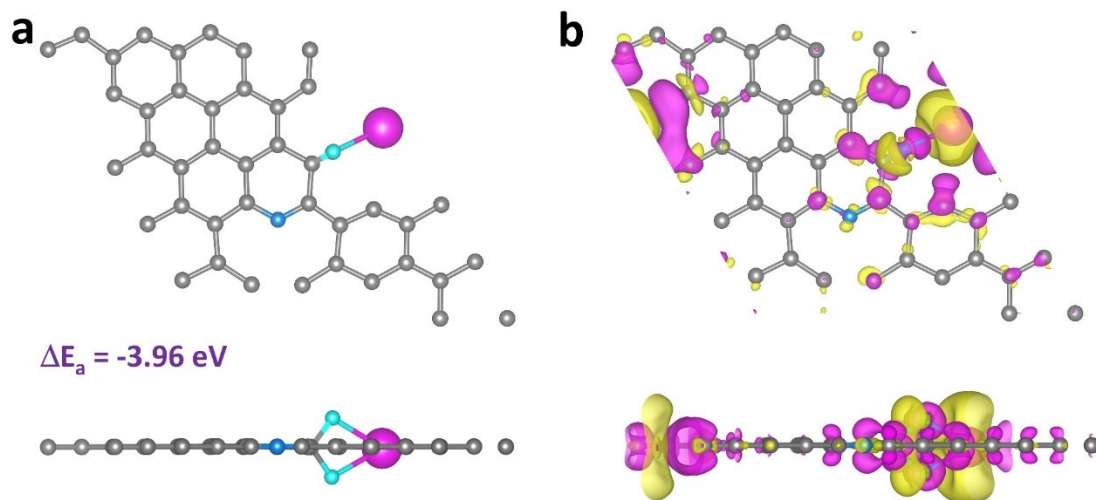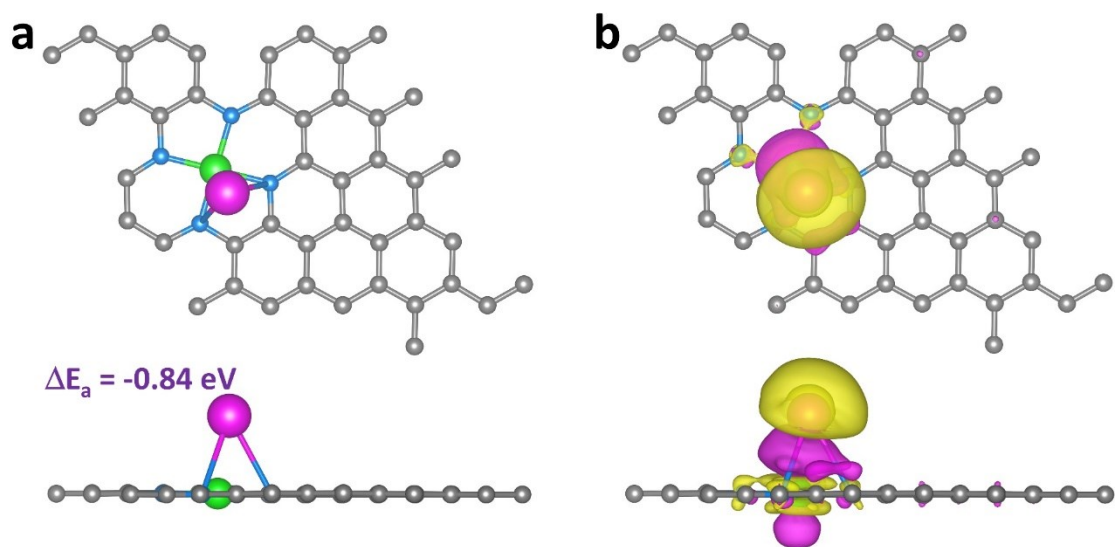
Figue S35. (a) Top and side illustration of simulations for a single Na ion adsorbed on the MnN$_4$-C and the corresponding ΔEa. (b) Calculated charge density differences of Na ion adsorbed on the MnN$_4$-C structure.
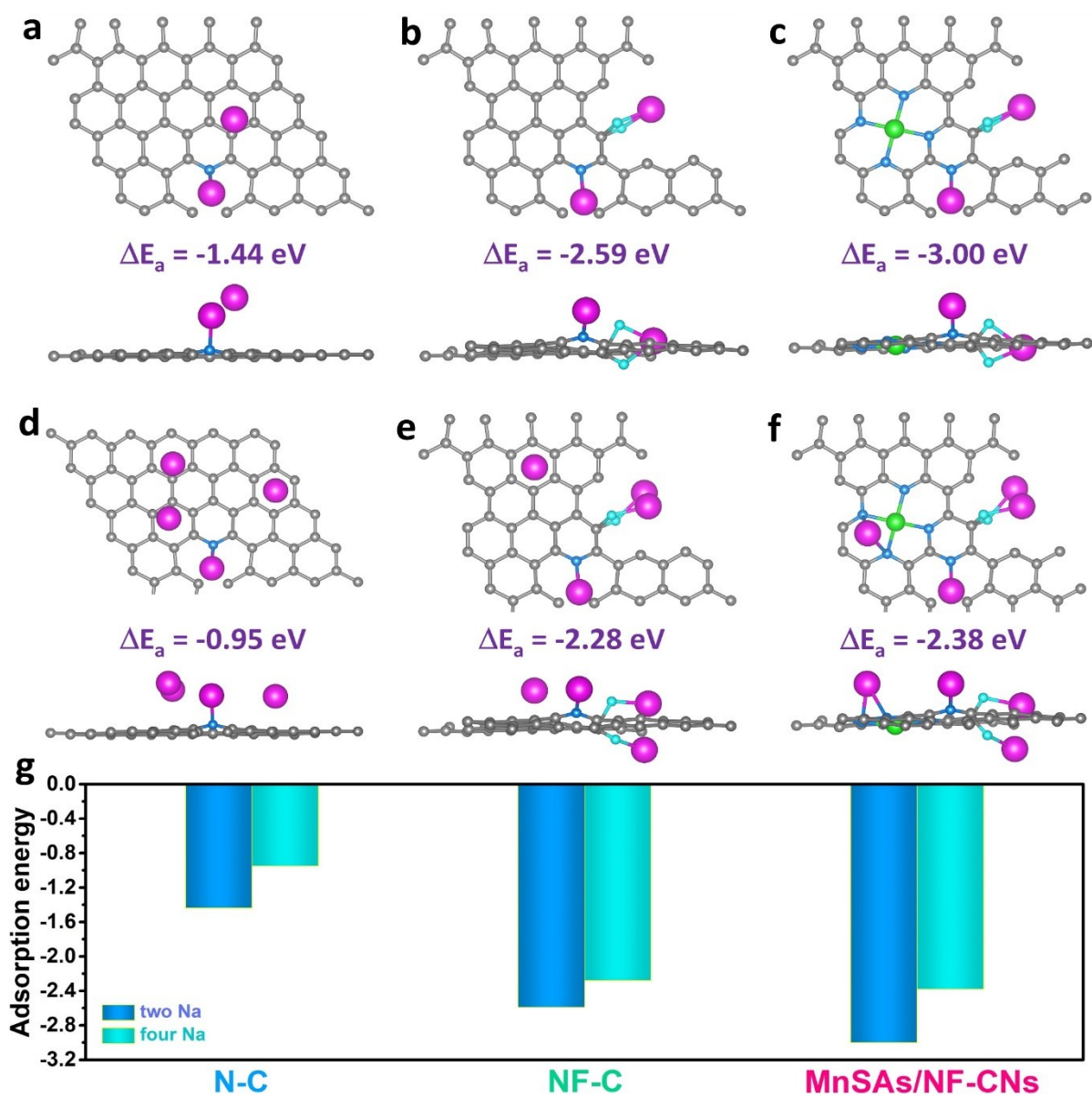
Figue S36. Top and side illustration of simulations for two and four Na ion adsorbed on the (a, d) N-C, (b, e) NF-C and (c, f) MnSAs/NF-CNs as well as their corresponding average ΔEa.
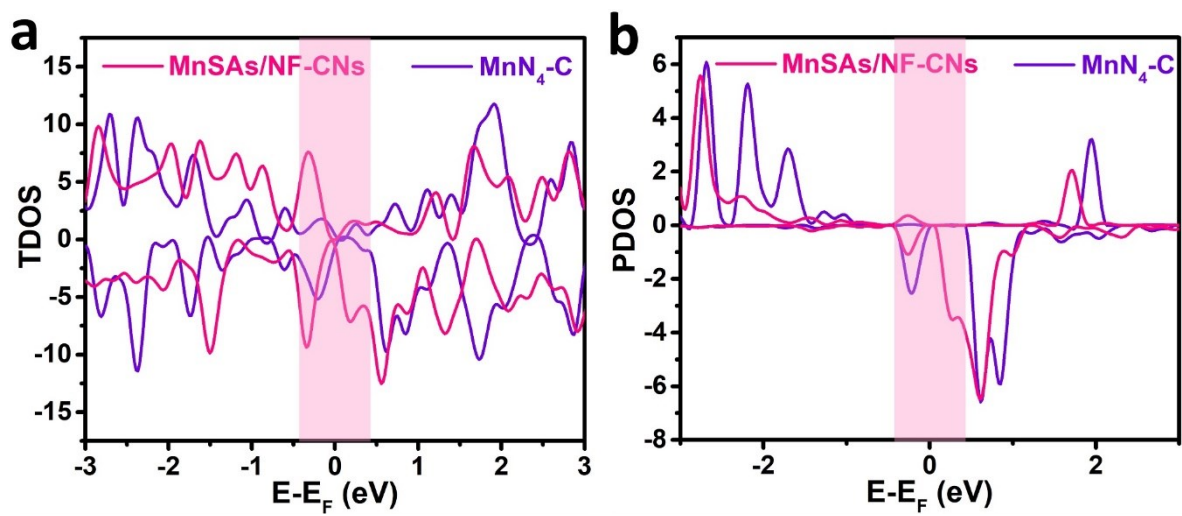
Figue S37. (a) The density of states and (b) p orbital partial density of states (PDOS) of MnSAs/NF-CNs and MnN$_4$-C structures.
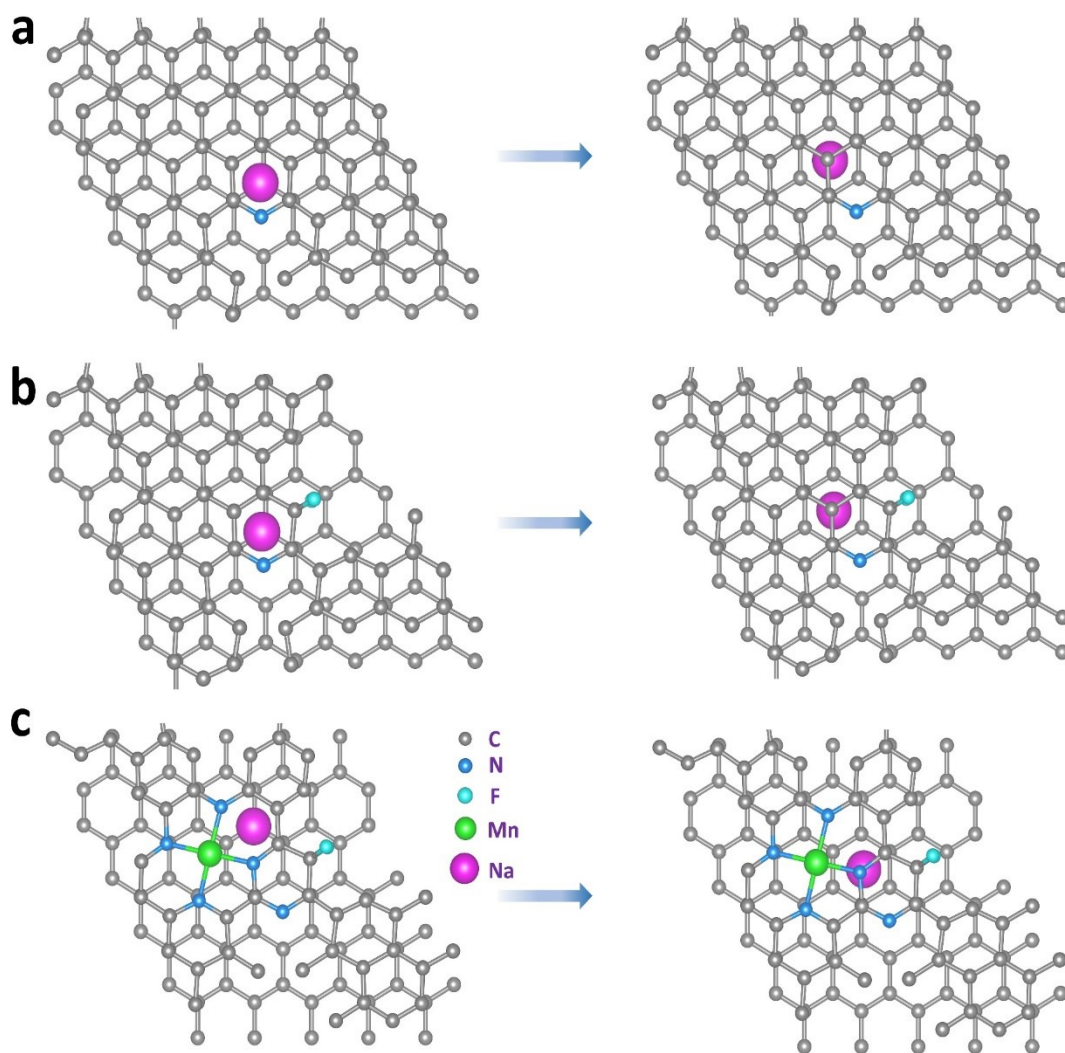
Figue S38. Illustration of the Na ion diffusion path from one hollow position to the nearest hollow position in (a) N-C, (b) NF-C and (c) MnSAs/NF-CNs.
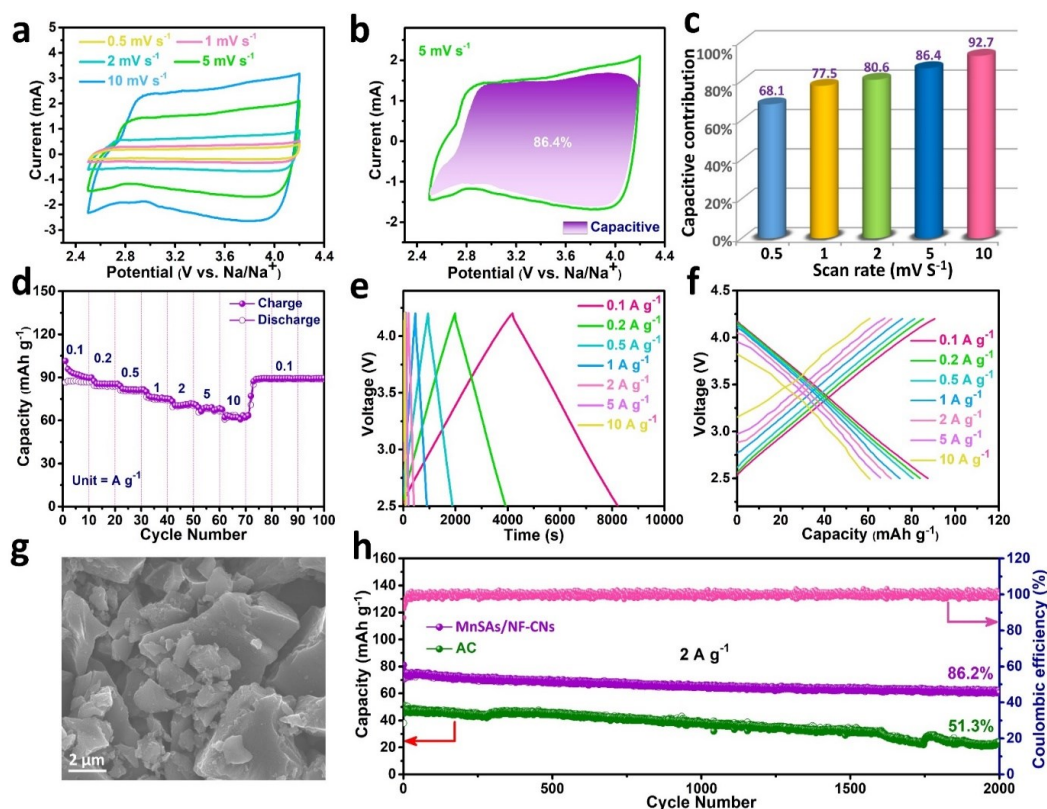
Figue S39. Electrochemical performance of MnSAs/NF-CNs cathode within a voltage window of 2.5 - 4.2 V versus Na metal. (a) Typical CV curves at different scan rates. (b) Capacitive controlled contributions at a scan rate of 5mV s^{-1}. (c) Ratios of surface capacitive contribution at di□erent scan rates. (d) Rate capability, (e) GCD curves and (f) charge/discharge curves at di□erent current densities. (g) SEM image of commercial AC. (h) Long-term cycle performance of MnSAs/NF-CNs and AC at 2 A g^{-1}.

Due to the large surface area and pore volume as well as highly hierarchical porosity, MnSAs/NF-CNs was employed as cathode material. It can be found that the contribution ratios of capacitive capacity gradually increased from 68.1% to 92.7% with the elevation of scan rates based on the above mentioned current separation method. Thus, the ClO$_4$$^-$ anions storage mechanism of MnSAs/NF-CNs mainly depend on the adsorption/desorption onto electrode surface and reversible reactions between electrolyte ions and heteroatoms, and a fraction of intercalation process. The MnSAs/NF-CNs cathode delivers a large average reversible specific capacity of 87 mAh g^{-1} at 0.1 A g^{-1}, which still maintained 63 mAh g^{-1} even at a high current density of 10 A g^{-1}, showing superior rate capability. Moreover, the capacity retention of the MnSAs/NF-CNs cathode can keep at 86.2% over 2000 cycles at 2 A g^{-1} with the Coulombic efficiency approach 99%, which is much superior to that of the commercial AC, demonstrating the ideal cathodic material candidate for constructing high-performance SIHCs.
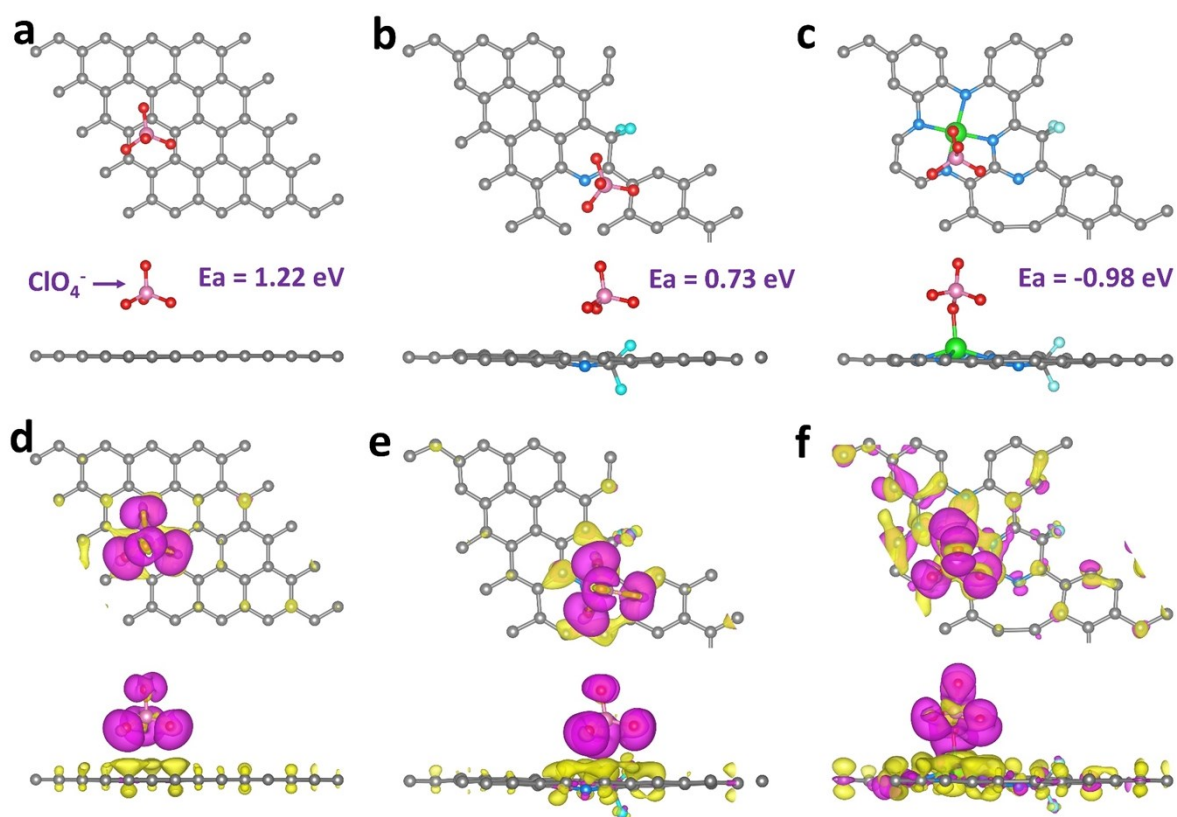
Figue S40. Top and side view of the ClO_4^- adsorbed on (a) commercial active carbon, (b) NF-C, (c) MnSAs/NF-CNs and the corresponding ΔEa. Top and side view of the calculated charge density difference of ClO_4^- adsorbed on (d) commercial active carbon, (e) NF-C and (f) MnSAs/NF-CNs.
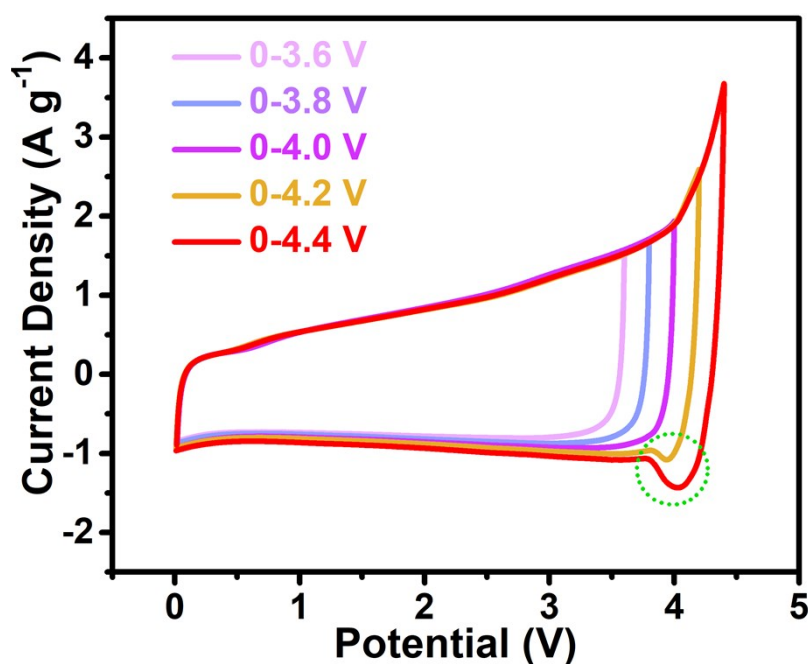
Figue S41. CV curves of the MnSAs/NF-CNs//MnSAs/NF-CNs SIHCs device in different potential windows at a scan rate of 20 mV s⁻¹. With increasing the cut-off potential window from 3.6 V to 4.2 V, current response enhances. However, significant side reactions are presented when the device operates at a maximum potential window up to 4.2 V. Thus, the appropriate operation window for the SIHCs device was 0 - 4V to avoid the decomposition of electrolyte and other side reactions.
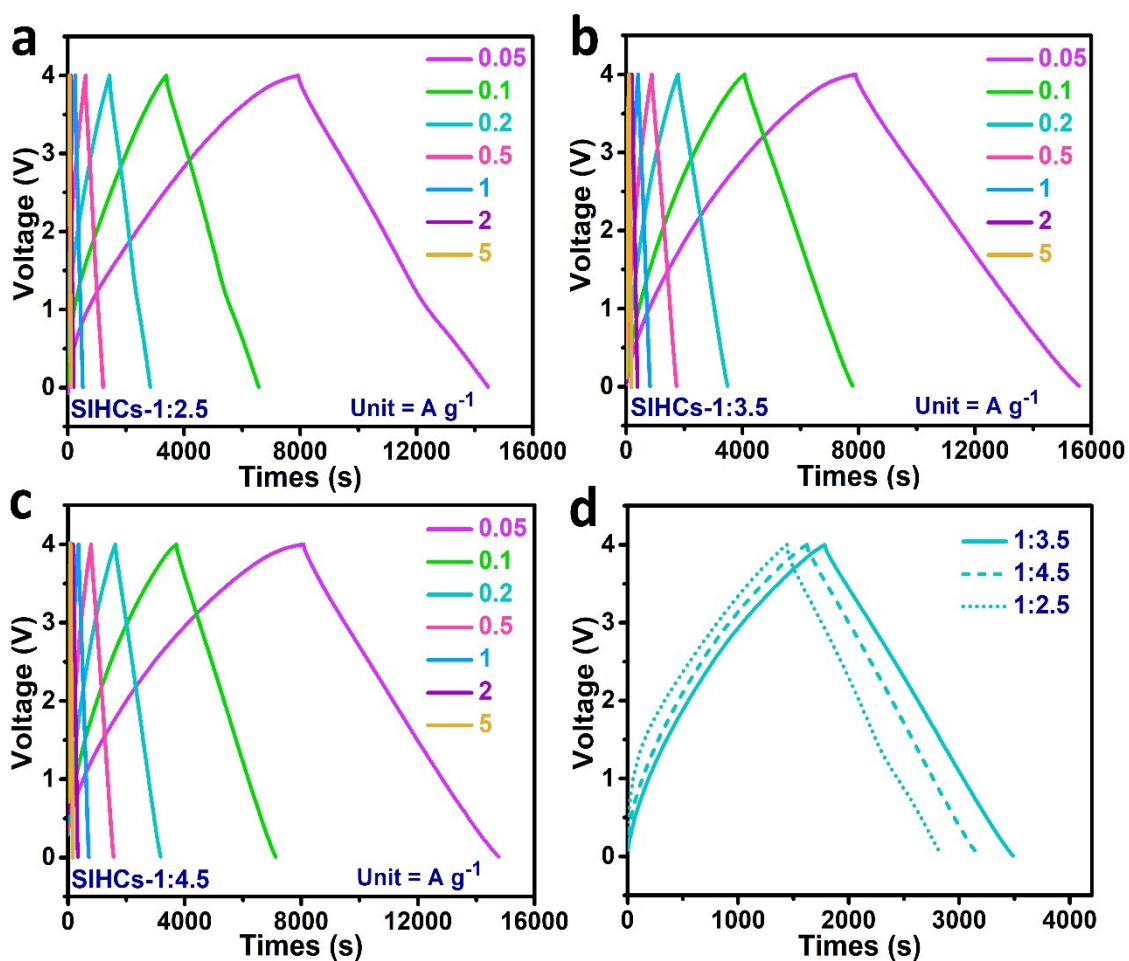
Figure S42. (a-c) Typical GCD curves of the MnSAs/NF-CNs//MnSAs/NF-CNs SIHCs with different mass ratios of anode/cathode at different current densities for the voltage window of 0 - 4.0 V. (d) GCD curves of SIHCs at 0.2 A g^{-1} with different anode/cathode mass radio.

The longest discharge time of the SIHCs with mass ratio of 1:3.5 indicates that it possesses the best electrochemical performance. The optimal mass ratio between the anode and cathode in the SIHCs also conform to the charge balance theory (Q^+ m^+ = Q^- m^-). Therefore, the MnSAs/NF-CNs//MnSAs/NF-CNs SIHCs with a mass ratio of 1:3.5 is selected for the succedent tests.
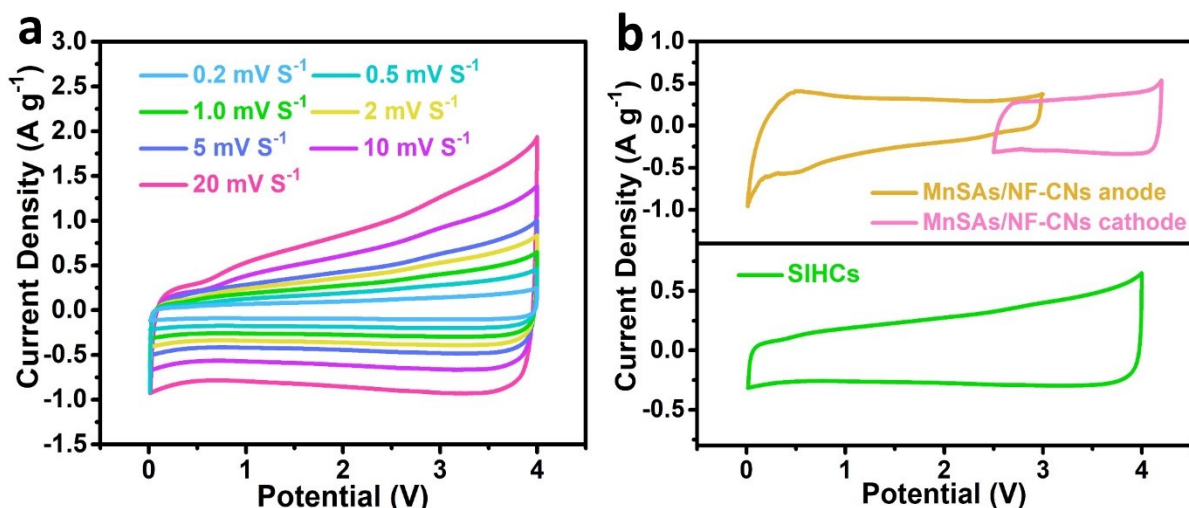
Figue S43. (a) CV curves at different scan rates of the MnSAs/NF-CNs//MnSAs/NF-CNs SIHCs device from 0.01 to 4.0 V. (b) CV curves of the MnSAs/NF-CNs anode and the MnSAs/NF-CNs cathode in half cells (top) and full cell of SIHCs (bottom) at 1 mV s^{-1}.

During the charging process, Na$^+$ cations are adsorbed/inserted the MnSAs/NF-CNs anode, while ClO$_4^-$ anions are adsorbed on the MnSAs/NF-CNs cathode surface. The discharge process of the SIHCs is vice versa. Due to the combination of two different charge storage mechanisms, no obvious redox peaks are observed in the CV curves of the SIHCs, implying a typical capacitor-like behavior. Moreover, the shape of the CV curve can still be maintained with the increasing scanning rate, demonstrating the high reversibility.
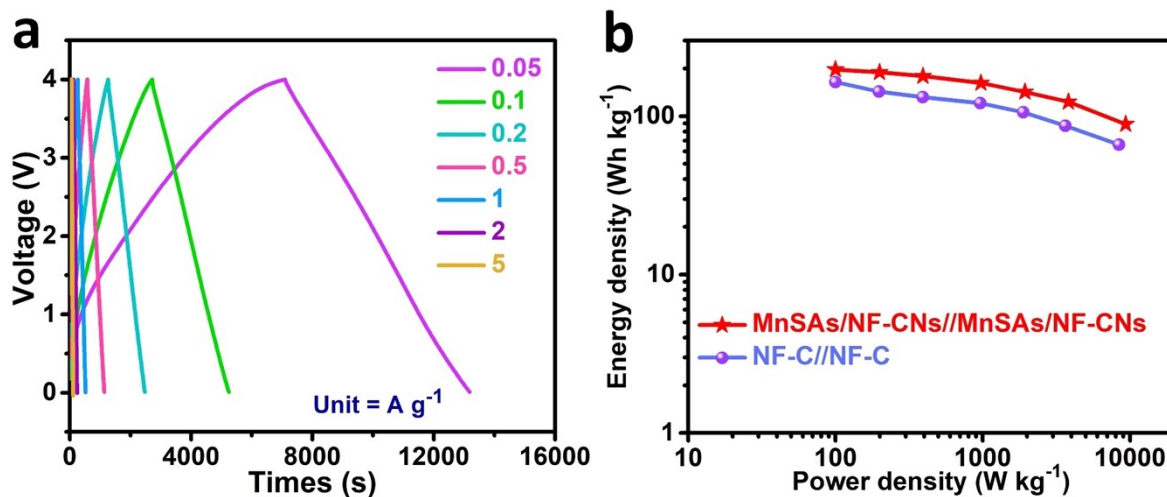
Figue 44. (a) Charge-discharge curves at diﬀerent current density of the NF-C//NF-C SIHCs device. (b) Ragone plots of the NF-C//NF-C compared with MnSAs/NF-CNs//MnSAs/NF-CNs SIHCs.
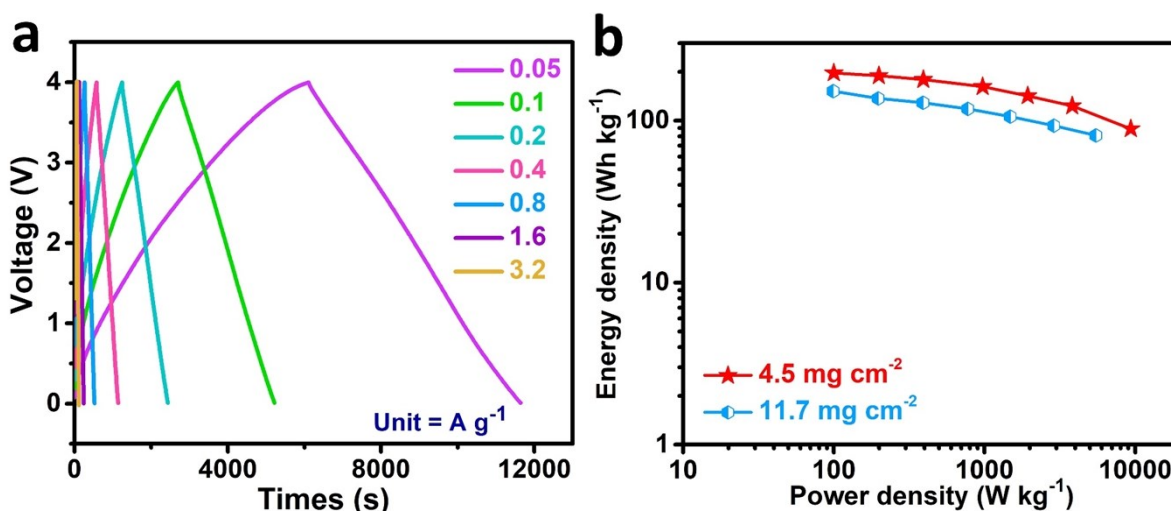
Figue 45. (a) Charge-discharge curves at di□erent current density of the MnSAs/NF-CNs//MnSAs/NF-CNs SIHCs with a high mass loading of 11.7 mg cm^{-2}. (b) Ragone plots of the MnSAs/NF-CNs//MnSAs/NF-CNs SIHCs with different mass loading.

The SIHCs full cells with material loading of 11.7 mg cm^{-2} (based on active materials of anode and cathode) can achieve a high energy density of 152 Wh kg^{-1} at the power density of 99 W kg^{-1}. Even at a high power density of 5476 W kg^{-1}, the SIHCs can still deliver a high energy density of 81 Wh kg^{-1}. These results clearly demonstrated that the mass loading did affect the electrochemical performance in terms of energy and power density to a certain extent. Reasonably, a high mass loading at working electrode tend to result in a lower utilization of electrode materials possibly due to increasing distance of mass transport or resistance of electron. Nevertheless, the SIHCs still displayed a desirable energy and power density even at a high mass loading.
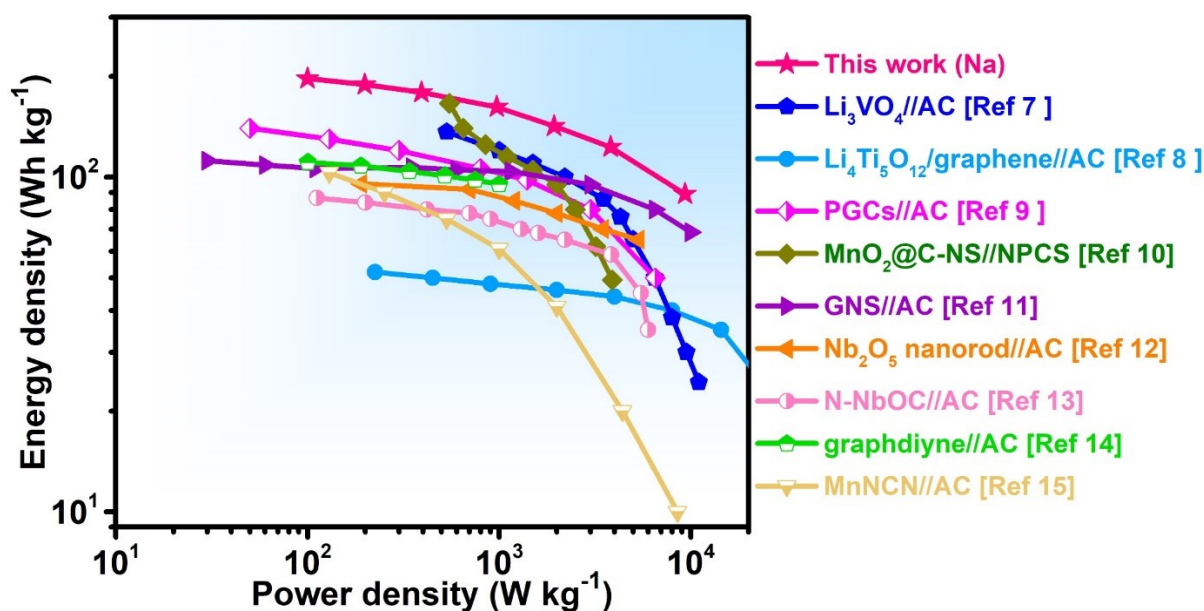
Figue S46. Ragone plot for MnSAs/NF-CNs//MnSAs/NF-CNs SIHCs device with comparison of previously reported lithium ion hybrid capacitors (LIHCs) in the literature.
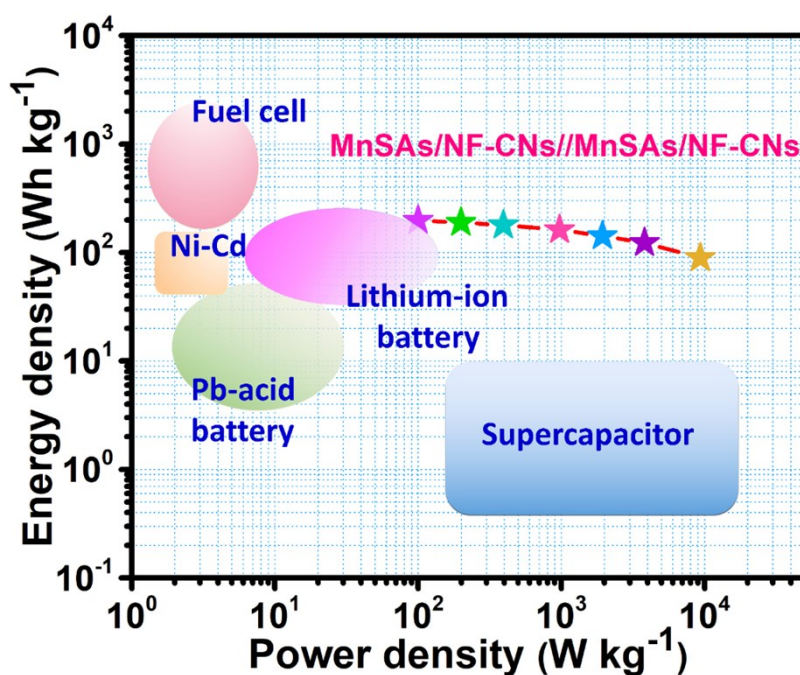
Figue S47. Ragone plots of the MnSAs/NF-CNs//MnSAs/NF-CNs SIHCs device as compared with commercial energy storage devices.
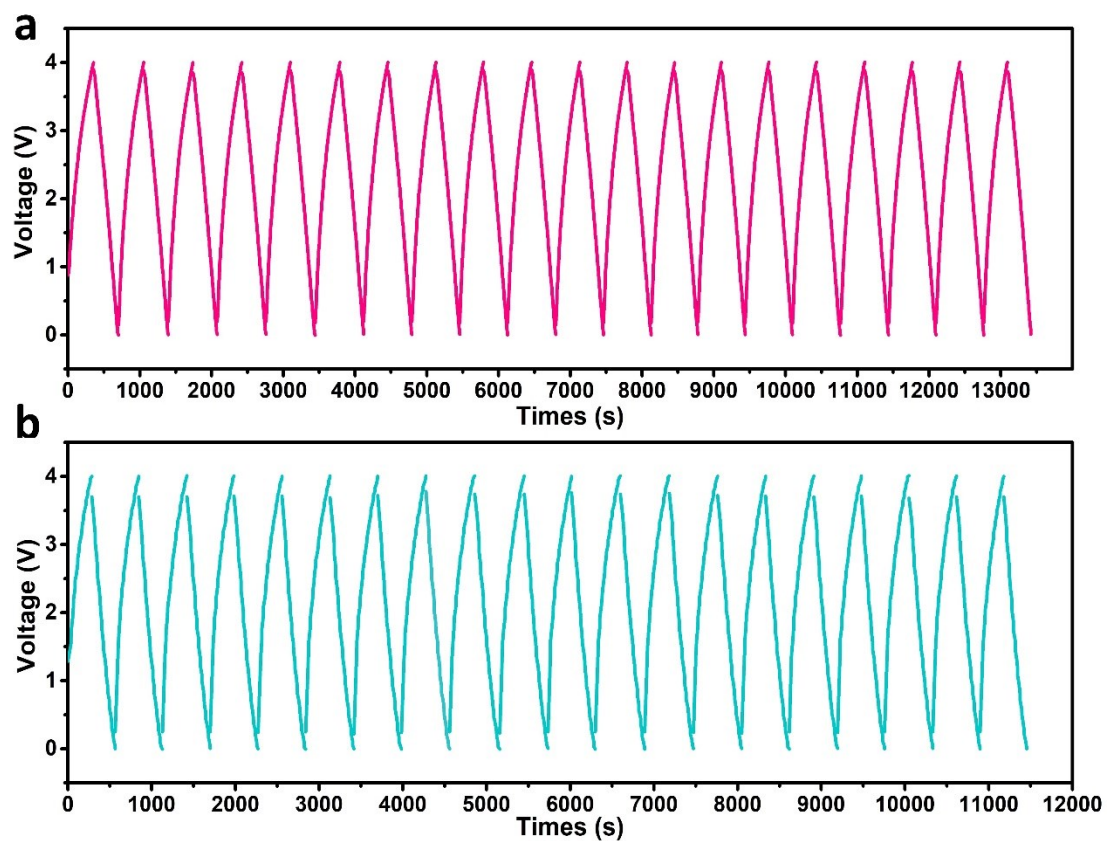
Figue S48. The charge-discharge profiles of the initial 20 cycles (a) and the final 20 cycles (b) of the MnSAs/NF-CNs//MnSAs/NF-CNs SIHCs device. The voltage/time curves exhibit a charge/discharge process without obvious distortion, demonstrating the excellent reversibility and perfect kinetics balance between the cathode and anode.
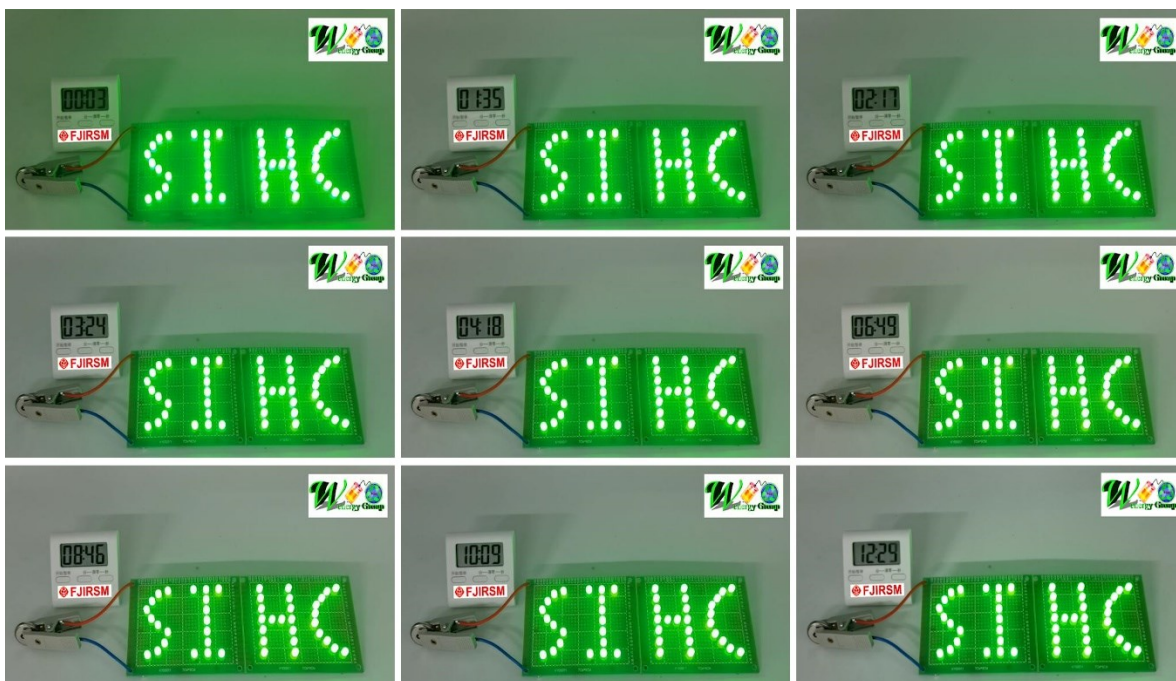
Figue S49. The MnSAs/NF-CNs//MnSAs/NF-CNs SIHCs device could power the LEDs pattern for over 10 min.

Table S1. X-ray photoelectron spectrum analysis of the MnSAs/NF-CNs, NF-C and N-C.

Sample	Element content/%(at%)				
	C	Mn	N	F	O
MnSAs/NF-CNs	65.35	9.27	19.06	1.61	4.71
NF-C	69.49	-	20.18	1.42	8.91
N-C	68.11	-	22.53	-	9.36

The content of Mn from the XPS analysis are slightly different from TG results, which might due to XPS analysis focuses on the top few nanometers of a sample.

Table S2. EXAFS fitting results of MnSAs/NF-CNs.

Sample	Path	N	R(Å)	σ^2(Å^2)	ΔE_0 (eV)	R-Factor	R-range (Å)	K-range (Å^{-1})	S_0^2
MnSAs/NF-CNs	Mn-N	4.0	2.14	0.0095	-0.54	0.0071	1.0-2.0	1-11	0.9

Note: N, coordination number; R, distance between absorber and backscatter atoms; σ^2, Debye-Waller factor to account for both thermal and structural disorders; ΔE_0, inner potential correction; R factor (%) indicates the goodness of the fit. Error bounds (accuracies) that characterize the structural parameters obtained by EXAFS spectroscopy were estimated as N $\pm$ 20%; R $\pm$ 1%; $\sigma2 \pm$ 20%; $\Delta E_0 \pm$ 20%. $S_0^2$was fixed to 0.90 as determined from bulk fitting. R-range and K-range were the fitting range for each sample.

Table S3. The cycling performance comparison of MnSAs/NF-CNs and previously reported state-of-art carbonaceous materials for SIBs.

Materials	Voltage range(V)	Current density (mA g⁻¹)	Cycle number	Specific capacity (mAh g⁻¹)	Reference
MnSAs/NF-CNs	0.01-3.0	200	300	326	This work
		5000	7000	224	
S-doped porous hard carbon	0.01-3.0	1000	4000	200	Ref 16
N-doped few-layer graphene	0.01-2.5	500	2000	211.3	Ref 17
Ultramicropores hard carbon nanosheets	0.01-1.5	100	100	126.6	Ref 18
S-N/C	0.01-3.0	1000	1000	211	Ref 19
C/g-C₃N₄	0.01-2.0	400	400	160	Ref 20
oxygen and nitrogen codoped holey graphene	0.01-3.0	5000	2000	179	Ref 21
reduced holey graphene oxide	0.01-3.0	2000	3000	163	Ref 22
CEM-G-8h	0.01-3.0	500	2000	140	Ref 23
N, B co-doping carbon nanosheets	0.01-3.0	200	200	309	Ref 24
Hard-soft carbon composite	0.01-2.5	150	100	191	Ref 25
hard carbon paper	0.01-2.0	2000	1000	176.8	Ref 26
Microporous hard carbon	0.01-2.7	1000	1000	113	Ref 27
expanded graphite	0.01-2.0	100	2000	136	Ref 28
N-rich porous carbon nanosheets	0.01-3.0	5000	1000	170	Ref 29

sulfurized polyacrylonitrile derived carbon	0.01-3.0	500	3000	152	Ref 30
nitrogen-doped carbon nanofiber	0.01-3.0	5000	7000	210	Ref 31
N/S codoped carbon microspheres	0.01-3.0	500	3400	150	Ref 32
soft carbon nanosheets	0.01-3.0	800	3500	128.7	Ref 33
highly ordered graphene solid	0.005-3.0	100	500	120	Ref 34
N-HC	0.01-3.0	200	200	214	Ref 35
N,O-codoped porous carbon nanosheets	0.001-3.0	700	1000	198.5	Ref 36
sulfur-doped graphene	0.001-3.0	1000	200	150	Ref 37
hard carbons	0.01-2.5	500	1000	200	Ref 38
N, S co-doped carbon	0.01-3.0	50	200	280	Ref 39
NHBCM	0.01-2.5	5000	1000	104	Ref 40
S, N, O-doped hard carbon nanosheets	0.001-3.0	1000	1000	177	Ref 41
N-doped carbon	0.01-2.8	2000	500	145	Ref 42
3D framework carbon	0.01-2.5	500	1000	175	Ref 43
CNFs-1300	0.001-2.5	200	100	233	Ref 44
HN-CSMCNs	0.01-3.0	500	1000	205	Ref 45

Table S4. The cycling performance comparison of MnSAs/NF-CNs and previously reported transition metal related anodes for SIBs.

Materials	Voltage range (V)	Current density (mA g^{-1})	Cycle number	Specific capacity (mAh g^{-1})	Reference
MnSAs/NF-CNs	0.01-3.0	200	300	326	This work
		5000	7000	224	
VS$_2$-SNSs	0.4-2.2	200	100	295	Ref 46
Na$_2$Ti$_2$O$_5$-VS$_2$	0.01-2.5	200	100	203	Ref 47
TiO$_2$@TiO$_{2-x}$-P	0.01-3.0	50	100	308	Ref 48
FeTiO$_3$⊂CNTs	0.01-3.0	2000	3500	210.5	Ref 49
S doped TiO$_2$	0.01-3.0	50	100	254.2	Ref 50
WS$_2$/CNT-rGO-200	0.01-3.0	200	100	252.9	Ref 51
Zn-PTCA	0.01-2.0	200	50	302	Ref 52
Ni$_{1.5}$Co$_{0.5}$P$_x$@F CNT-FS	0.01-3.0	1000	100	188.9	Ref 53
Cu3P/CNS	0.01-2.8	1000	100	150.9	Ref 54
Ni$_2$P/NG/Ni$_2$P	0.01-2.5	1000	400	107.8	Ref 55

Table S5. Bader charge analysis of the samples.

Sample	Average charge state (e)			
	F	N	Mn	Na
NF-C-Na	7.749(+0.749)	7.914(+2.914)	-	8.142(-0.858)
MnSAs/NF-CNs-Na	7.796(+0.796)	8.039(+3.039)	13.514(-1.486)	8.106(-0.894)
Mn-N$_4$-C	-	-	13.580(-1.420)	-
Mn-N$_4$-C-Na	-	-	13.898(-1.102)	8.334(-0.666)

Table S6. The cycling performance comparison of MnSAs/NF-CNs//MnSAs/NF-CNs SIHCs and previously reported SIHCs.

SIHCs	Current Density (mA g^{-1})	Cycle number	capacity retention (%)	Reference
MnSAs/NF-CNs//MnSAs/NF-CNs	1000	10000	85.2	This work
VO$_2$@mp-CNSs//NVP@mp-CNSs/CFC	1000	2000	78	Ref 56
SnS$_2$/GCA//activated Ketjenblack	1000	1500	68.4	Ref 57
TiO$_2$@CNT@C//activated carbon	1000	5000	85.3	Ref 58
Disordered carbon//macroporous graphene	1000	1200	85	Ref 59
Na$_3$V$_2$(PO$_4$)$_3$//bulk Na$_3$V$_2$(PO$_4$)$_3$	1170	10000	64.5	Ref 60
Na$_2$Ti$_3$O$_7$/carbon textiles//GF	500	2500	80.3	Ref 61
hard carbon//activated carbon	400	10000	70	Ref 62
FeVO$_4$·0.6H$_2$O//NVOPF/rGO	1000	5000	60	Ref 63
disordered carbon nanoparticles//NC	300	1000	70	Ref 64
rGO/AC//Na$_2$Ti$_2$O$_{5-x}$//rGO/AC	1000	5000	82.5	Ref 65
Nb$_2$O$_5$//peanut shell carbon	1280	3000	80	Ref 66
OCG//OCG	500	2500	86.7	Ref 67

TiO$_2$/MoS$_2$@NC-800-7//AC	200	400	81	Ref 68
Ti(O,N)//AC	1000	1000	82.9	Ref 69
Na$_{0.77}$MnO$_2$·0.5H$_2$O/C//graphite	1000	100	72	Ref 70
TiO$_{2-S}$//Na$_2$V$_3$(PO$_4$)$_3$	1000	1000	83	Ref 71
FeVO//Na$_3$(VO)$_2$(PO$_4$)$_2$F	1200	9000	68	Ref 72
M-TiO$_2$@rGO//HPAC	1000	10000	84.7	Ref 73
TiO$_{2-x}$/CNT//AC/CNT	1000	2000	73	Ref 74
Na$_2$Ti$_2$O$_5$//AC	640	10000	72.9	Ref 75

Supporting References

[1]   E. Lim, H. Kim, C. Jo, J. Chun, K. Ku, S. Kim, H. I. Lee, I. S. Nam, S. Yoon, K. Kang, J. Lee, *ACS nano* **2014**, *8*, 8968-8978.

[2]   P. Giannozzi, S. Baroni, N. Bonini, M. Calandra, R. Car, C. Cavazzoni, D. Ceresoli, G. L. Chiarotti, M. Cococcioni, I. Dabo, A. Dal Corso, S. de Gironcoli, S. Fabris, G. Fratesi, R. Gebauer, U. Gerstmann, C. Gougoussis, A. Kokalj, M. Lazzeri, L. Martin-Samos, N. Marzari, F. Mauri, R. Mazzarello, S. Paolini, A. Pasquarello, L. Paulatto, C. Sbraccia, S. Scandolo, G. Sclauzero, A. P. Seitsonen, A. Smogunov, P. Umari, R. M. Wentzcovitch, *Journal of physics. Condensed matter : an Institute of Physics journal* **2009**, *21*, 395502.

[3]   B. Ravel, M. Newville, *Journal of synchrotron radiation* **2005**, *12*, 537-541.

[4]   Y. Fang, D. Luan, Y. Chen, S. Gao, X. W. D. Lou, *Angewandte Chemie* **2020**, *59*, 2644-2648.

[5]   X. Hu, X. Sun, S. J. Yoo, B. Evanko, F. Fan, S. Cai, C. Zheng, W. Hu, G. D. Stucky, *Nano Energy* **2019**, *56*, 828-839.

[6]   Z. Hong, Y. Zhen, Y. Ruan, M. Kang, K. Zhou, J. M. Zhang, Z. Huang, M. Wei, *Adv Mater* **2018**, *30*, e1802035.

[7]   G. K. Wang, C. X. Lu, X. Zhang, B. A. Wan, H. Y. Liu, M. R. Xia, H. Y. Gou, G. Q. Xin, J. Lian, Y. G. Zhang, *Nano Energy* **2017**, *36*, 46-57.

[8]   L. Shen, H. Lv, S. Chen, P. Kopold, P. A. van Aken, X. Wu, J. Maier, Y. Yu, *Adv Mater* **2017**, *29*.

[9]   G. Li, Z. Yin, H. Guo, Z. Wang, G. Yan, Z. Yang, Y. Liu, X. Ji, J. Wang, *Advanced Energy Materials* **2019**, *9*, 1802878.

[10]   D. P. Dubal, K. Jayaramulu, J. Sunil, Š. Kment, P. Gomez-Romero, C. Narayana, R. Zbořil, R. A. Fischer, *Advanced Functional Materials* **2019**, *29*, 1900532.

[11]   G. Li, Y. Huang, Z. Yin, H. Guo, Y. Liu, H. Cheng, Y. Wu, X. Ji, J. Wang, *Energy Storage Materials* **2020**, *24*, 304-311.

[12]   B. Deng, T. Lei, W. Zhu, L. Xiao, J. Liu, *Advanced Functional Materials* **2018**, *28*, 1704330.

[13]   S. Hemmati, G. Li, X. Wang, Y. Ding, Y. Pei, A. Yu, Z. Chen, *Nano Energy* **2019**, *56*, 118-126.

[14]   H. P. Du, H. Yang, C. S. Huang, J. J. He, H. B. Liu, Y. L. Li, *Nano Energy* **2016**, *22*, 615-622.

[15] C. F. Liu, C. K. Zhang, H. Y. Fu, X. H. Nan, G. Z. Cao, *Advanced Energy Materials* **2017**, *7*, 1601127.

[16] Z. Hong, Y. Zhen, Y. Ruan, M. Kang, K. Zhou, J. M. Zhang, Z. Huang, M. Wei, *Adv Mater* **2018**, *30*, e1802035.

[17] J. Liu, Y. Zhang, L. Zhang, F. Xie, A. Vasileff, S. Z. Qiao, *Adv Mater* **2019**, *31*, 1901261.

[18] J. L. Xia, D. Yan, L. P. Guo, X. L. Dong, W. C. Li, A. H. Lu, *Adv Mater* **2020**, *32*, 2000447.

[19] J. Yang, X. Zhou, D. Wu, X. Zhao, Z. Zhou, *Adv Mater* **2017**, *29*, 1604108.

[20] G. M. Weng, Y. Xie, H. Wang, C. Karpovich, J. Lipton, J. Zhu, J. Kong, L. D. Pfefferle, A. D. Taylor, *Angewandte Chemie* **2019**, *58*, 13727-13733.

[21] J. Zhao, Y. Z. Zhang, J. Y. Chen, W. L. Zhang, D. Yuan, R. Chua, H. N. Alshareef, Y. W. Ma, *Advanced Energy Materials* **2020**, *10*, 2000099.

[22] J. Zhao, Y.-Z. Zhang, F. Zhang, H. Liang, F. Ming, H. N. Alshareef, Z. Gao, *Advanced Energy Materials* **2019**, *9*, 1803215.

[23] X. Zhao, Y. Ding, Q. Xu, X. Yu, Y. Liu, H. Shen, *Advanced Energy Materials* **2019**, *9*, 1803648.

[24] Q. Jin, W. Li, K. Wang, H. Li, P. Feng, Z. Zhang, W. Wang, K. Jiang, *Advanced Functional Materials* **2020**, *30*, 1909907.

[25] F. Xie, Z. Xu, A. C. S. Jensen, H. Au, Y. Lu, V. Araullo-Peters, A. J. Drew, Y. S. Hu, M. M. Titirici, *Advanced Functional Materials* **2019**, *29*, 1901072.

[26] B. H. Hou, Y. Y. Wang, Q. L. Ning, W. H. Li, X. T. Xi, X. Yang, H. J. Liang, X. Feng, X. L. Wu, *Advanced Materials* **2019**, *31*, e1903125.

[27] Z. L. Yu, S. Xin, Y. You, L. Yu, Y. Lin, D. W. Xu, C. Qiao, Z. H. Huang, N. Yang, S. H. Yu, J. B. Goodenough, *Journal of the American Chemical Society* **2016**, *138*, 14915-14922.

[28] Y. Wen, K. He, Y. Zhu, F. Han, Y. Xu, I. Matsuda, Y. Ishii, J. Cumings, C. Wang, *Nature communications* **2014**, *5*, 4033.

[29] S. T. Liu, J. S. Zhou, H. H. Song, *Advanced Energy Materials* **2018**, *8*, 1800569.

[30] J. Qian, F. Wu, Y. Ye, M. Zhang, Y. Huang, Y. Xing, W. Qu, L. Li, R. Chen, *Advanced Energy Materials* **2018**, *8*, 1703159.

[31] S. Wang, L. Xia, L. Yu, L. Zhang, H. Wang, X. W. D. Lou, *Advanced Energy Materials* **2016**, *6*, 1502217.

[32] D. Xu, C. Chen, J. Xie, B. Zhang, L. Miao, J. Cai, Y. Huang, L. Zhang, *Advanced Energy Materials* **2016**, *6*, 1501929.

[33] X. Yao, Y. Ke, W. Ren, X. Wang, F. Xiong, W. Yang, M. Qin, Q. Li, L. Mai, *Advanced Energy Materials* **2018**, *9*, 1803260.

[34] H. Ma, H. Geng, B. Yao, M. Wu, C. Li, M. Zhang, F. Chi, L. Qu, *ACS nano* **2019**, *13*, 9161-9170.

[35] X. Hu, X. Sun, S. J. Yoo, B. Evanko, F. Fan, S. Cai, C. Zheng, W. Hu, G. D. Stucky, *Nano Energy* **2019**, *56*, 828-839.

[36] J. Niu, J. J. Liang, R. Shao, M. Y. Liu, M. L. Dou, Z. L. Li, Y. Q. Huang, F. Wang, *Nano Energy* **2017**, *41*, 285-292.

[37] X. Wang, G. Li, F. M. Hassan, J. Li, X. Fan, R. Batmaz, X. Xiao, Z. Chen, *Nano Energy* **2015**, *15*, 746-754.

[38] P. Bai, Y. He, P. Xiong, X. Zhao, K. Xu, Y. Xu, *Energy Storage Materials* **2018**, *13*, 274-282.

[39] Q. Jin, K. Wang, P. Feng, Z. Zhang, S. Cheng, K. Jiang, *Energy Storage Materials* **2020**, *27*, 43-50.

[40] W. Xiong, Z. Wang, J. Zhang, C. Shang, M. Yang, L. He, Z. Lu, *Energy Storage Materials* **2017**, *7*, 229-235.

[41] J. Yang, S. Xiao, X. Cui, W. Dai, X. Lian, Z. Hao, Y. Zhao, J.-S. Pan, Y. Zhou, L. Wang, W. Chen, *Energy Storage Materials* **2020**, *26*, 391-399.

[42] S. Liu, J. Zhou, H. Song, *Small* **2018**, *14*, 1703548.

[43] B. Yang, J. Chen, S. Lei, R. Guo, H. Li, S. Shi, X. Yan, *Advanced Energy Materials* **2018**, *8*, 1702409.

[44] H. Yang, R. Xu, Y. Yu, *Energy Storage Materials* **2019**, *22*, 105-112.

[45] J. Mao, D. Niu, N. Jiang, G. Jiang, M. Chen, Y. Li, J. Shi, *Journal of Materials Chemistry A* **2020**, *8*, 9768-9775.

[46] R. Sun, Q. Wei, J. Sheng, C. Shi, Q. An, S. Liu, L. Mai, *Nano Energy* **2017**, *35*, 396-404.

[47] J.-Y. Liao, A. Manthiram, *Nano Energy* **2015**, *18*, 20-27.

[48] Q. Gan, H. He, Y. Zhu, Z. Wang, N. Qin, S. Gu, Z. Li, W. Luo, Z. Lu, *ACS nano* **2019**, *13*, 9247-9258.

[49] L. Yu, J. Liu, X. Xu, L. Zhang, R. Hu, J. Liu, L. Ouyang, L. Yang, M. Zhu, *ACS nano* **2017**, *11*, 5120-5129.

[50] H. He, D. Huang, W. Pang, D. Sun, Q. Wang, Y. Tang, X. Ji, Z. Guo, H. Wang, *Advanced Materials* **2018**, *30*, e1801013.

[51] Y. Wang, D. Z. Kong, W. H. Shi, B. Liu, G. J. Sim, Q. Ge, H. Y. Yang, *Advanced Energy Materials* **2016**, *6*, 1601057.

[52] Y. J. Liu, X. L. Zhao, C. Fang, Z. Ye, Y. B. He, D. N. Lei, J. Yang, Y. Zhang, Y. Y. Li, Q. Liu, Y. Huang, R. Zeng, L. T. Kang, J. J. Liu, Y. H. Huang, *Chem* **2018**, *4*, 2463-2478.

[53] X.-W. Wang, H.-P. Guo, J. Liang, J.-F. Zhang, B. Zhang, J.-Z. Wang, W.-B. Luo, H.-K. Liu, S.-X. Dou, *Advanced Functional Materials* **2018**, *28*, 1801016.

[54] M. Kong, H. Song, J. Zhou, *Advanced Energy Materials* **2018**, *8*, 1801489.

[55] C. Dong, L. Guo, Y. He, C. Chen, Y. Qian, Y. Chen, L. Xu, *Energy Storage Materials* **2018**, *15*, 234-241.

[56] D. M. Xu, D. L. Chao, H. W. Wang, Y. S. Gong, R. Wang, B. B. He, X. L. Hu, H. J. Fan, *Advanced Energy Materials* **2018**, 8, 1702769.

[57] J. Cui, S. Yao, Z. Lu, J.-Q. Huang, W. G. Chong, F. Ciucci, J.-K. Kim, *Advanced Energy Materials* **2018**, 8, 1702488.

[58] Y. E. Zhu, L. P. Yang, J. Sheng, Y. N. Chen, H. C. Gu, J. P. Wei, Z. Zhou, *Advanced Energy Materials* **2017**, 7, 1701222.

[59] F. Wang, X. Wang, Z. Chang, X. Wu, X. Liu, L. Fu, Y. Zhu, Y. Wu, W. Huang, *Adv Mater* **2015**, 27, 6962.

[60] Z. Jian, V. Raju, Z. Li, Z. Xing, Y.-S. Hu, X. Ji, *Advanced Functional Materials* **2015**, 25, 5778.

[61] S. Dong, L. Shen, H. Li, G. Pang, H. Dou, X. Zhang, *Advanced Functional Materials* **2016**, 26, 3703.

[62] Z. Xu, M. Wu, Z. Chen, C. Chen, J. Yang, T. Feng, E. Paek, D. Mitlin, *Adv Sci* **2019**, 6, 1802272.

[63] J. Dong, Y. He, Y. Jiang, S. Tan, Q. Wei, F. Xiong, Z. Chu, Q. An, L. Mai, *Nano Energy* **2020**, 73, 104838. 63.

[64] C. Wang, F. Wang, Z. Liu, Y. Zhao, Y. Liu, Q. Yue, H. Zhu, Y. Deng, Y. Wu, D. Zhao, *Nano Energy* **2017**, 41, 674.

[65] L.-F. Que, F.-D. Yu, K.-W. He, Z.-B. Wang, D.-M. Gu, *Chem Mater* **2017**, 29, 9133.

[66] H. Li, Y. Zhu, S. Dong, L. Shen, Z. Chen, X. Zhang, G. Yu, *Chem Mater* **2016**, 28, 5753.

[67] S. Dong, Y. Xu, L. Wu, H. Dou, X. Zhang, *Energy Storage Materials* **2018**, 11, 8-15.

[68]   Y. Z. Li, H. W. Wang, L. B. Wang, R. Wang, B. B. He, Y. S. Gong, X. L. Hu, *Energy Storage Materials* **2019**, 23, 95-104.

[69]   J. Dong, Y. Jiang, Q. Li, Q. Wei, W. Yang, S. Tan, X. Xu, Q. An, L. Mai, *Journal of Materials Chemistry A* **2017**, 5, 10827.

[70]   Y. L. Jiang, S. S. Tan, Q. L. Wei, J. Dong, Q. D. Li, F. Y. Xiong, J. Z. Sheng, Q. Y. An, L. Q. Mai, *Journal of Materials Chemistry A* **2018**, 6, 12259.

[71]   M. Kang, Y. Wu, X. Huang, K. Zhou, Z. Huang, Z. Hong, *Journal of Materials Chemistry A* **2018**, 6, 22840.

[72]   Q. Wei, Q. Li, Y. Jiang, Y. Zhao, S. Tan, J. Dong, L. Mai, D.-L. Peng, *Nano-Micro Letters* **2021**, 13. 72.

[73]   Y. Fang, Y. Zhang, C. Miao, K. Zhu, Y. Chen, F. Du, J. Yin, K. Ye, K. Cheng, J. Yan, G. Wang, D. Cao, *Nano-Micro Letters* **2020**, 12.

[74]   L. F. Que, F. D. Yu, Z. B. Wang, D. M. Gu, *Small* **2018**, 14, 1704508.

[75]   Q. Gui, D. Ba, Z. Zhao, Y. Mao, W. Zhu, T. Lei, J. Tan, B. Deng, L. Xiao, Y. Li, J. Liu, *Small Methods* **2019**, 3, 1800371.